Title

A novel role for osteopontin in macrophage-mediated amyloid-β clearance in Alzheimer's models

Authors

Rentsendorj, Altan
Sheyn, Julia
Fuchs, Dieu-Trang
et al.

Publication Date

2018

DOI

10.1016/j.bbi.2017.08.019

Peer reviewed

Brain, Behavior, and Immunity 67 (2018) 163–180

Contents lists available at ScienceDirect

Brain, Behavior, and Immunity

journal homepage: www.elsevier.com/locate/ybrbi

Full-length Article

A novel role for osteopontin in macrophage-mediated amyloid-β clearance in Alzheimer's models

Altan Rentsendorj [a], Julia Sheyn [a], Dieu-Trang Fuchs [a], David Daley [a], Brenda C. Salumbides [a], Hannah E. Schubloom [a], Nadav J. Hart [a], Songlin Li [a,b], Eric Y. Hayden [c], David B. Teplow [c], Keith L. Black [a], Yosef Koronyo [a], Maya Koronyo-Hamaoui [a,d,*]

[a] Department of Neurosurgery, Maxine Dunitz Neurosurgical Institute, Cedars-Sinai Medical Center, 127 S. San Vicente Blvd., Los Angeles, CA 90048, USA
[b] Institute of Life Sciences, Wenzhou University, 276 Xueyuan Middle Rd, Lucheng Qu, Wenzhou Shi, Zhejiang Sheng 325027, China
[c] Department of Neurology, David Geffen School of Medicine at UCLA, Mary S. Easton Center for Alzheimer's Disease Research at UCLA, Brain Research Institute, Molecular Biology Institute, University of California, 635 Charles E. Young Dr. S., Los Angeles, CA 90095, USA
[d] Department of Biomedical Sciences, Division of Applied Cell Biology and Physiology, Cedars-Sinai Medical Center, 127 S. San Vicente Blvd., Los Angeles, CA 90048, USA

ARTICLE INFO

Article history:
Received 24 January 2017
Received in revised form 11 August 2017
Accepted 28 August 2017
Available online 30 August 2017

Keywords:
Neurodegeneration
Neuroinflammation
SPP1
ETA-1
Vascular amyloid

ABSTRACT

Osteopontin (OPN), a matricellular immunomodulatory cytokine highly expressed by myelomonocytic cells, is known to regulate immune cell migration, communication, and response to brain injury. Enhanced cerebral recruitment of monocytes achieved through glatiramer acetate (GA) immunization or peripheral blood enrichment with bone marrow (BM)-derived $CD115^+$ monocytes (Mo^{BM}) curbs amyloid β-protein (Aβ) neuropathology and preserves cognitive function in murine models of Alzheimer's disease (ADtg mice). To elucidate the beneficial mechanisms of these immunomodulatory approaches in AD, we focused on the potential role of OPN in macrophage-mediated Aβ clearance. Here, we found extensive OPN upregulation along with reduction of vascular and parenchymal Aβ burden in cortices and hippocampi of GA-immunized ADtg mice. Treatment combining GA with blood-grafted Mo^{BM} further increased OPN levels surrounding residual Aβ plaques. In brains from AD patients and ADtg mice, OPN was also elevated and predominantly expressed by infiltrating GFP^+- or $Iba1^+$-$CD45^{high}$ monocyte-derived macrophages engulfing Aβ plaques. Following GA immunization, we detected a significant increase in a subpopulation of inflammatory blood monocytes ($CD115^+CD11b^+Ly6C^{high}$) expressing OPN, and subsequently, an elevated population of OPN-expressing $CD11b^+Ly6C^+CD45^{high}$ monocyte/macrophages in the brains of these ADtg mice. Correlogram analyses indicate a strong linear correlation between cerebral OPN levels and macrophage infiltration, as well as a tight inverse relation between OPN and Aβ-plaque burden. In vitro studies corroborate in vivo findings by showing that GA directly upregulates OPN expression in BM-derived macrophages ($M\Phi^{BM}$). Further, OPN promotes a phenotypic shift that is highly phagocytic (increased uptake of Aβ fibrils and surface scavenger receptors) and anti-inflammatory (altered cell morphology, reduced iNOS, and elevated IL-10 and Aβ-degrading enzyme MMP-9). Inhibition of OPN expression in $M\Phi^{BM}$, either by siRNA, knockout (KO^{OPN}), or minocycline, impairs uptake of Aβ fibrils and hinders GA's neuroprotective effects on macrophage immunological profile. Addition of human recombinant OPN reverses the impaired Aβ phagocytosis in KO^{OPN}-$M\Phi^{BM}$. This study demonstrates that OPN has an essential role in modulating macrophage immunological profile and their ability to resist pathogenic forms of Aβ.

1. Introduction

Osteopontin (OPN; encoded by the gene secreted phosphoprotein 1, SPP1) is a multifunctional matricellular glycoprotein secreted by a variety of activated immune cells such as macrophages and T cells, among other cell types (Franzen and Heinegard, 1985; Patarca et al., 1989; Scatena et al., 2007). It is highly expressed by bone marrow (BM)-derived myelomonocytic cells and modulates their migration, communication, and immunological responses (Lund et al., 2009; Rittling, 2011). Recent studies indicate that this glycoprotein may curb the pathology of various brain diseases such as stroke, ischemia, and traumatic brain injury via neuroprotective and repair-promoting effects (Brown, 2012;

* Corresponding author at: Departments of Neurosurgery and Biomedical Sciences, Cedars-Sinai Medical Center, Los Angeles, CA 90048, USA.
E-mail address: maya.koronyo@csmc.edu (M. Koronyo-Hamaoui).

http://dx.doi.org/10.1016/j.bbi.2017.08.019
0889-1591/

Chan et al., 2014; Gliem et al., 2015; Meller et al., 2005; van Velthoven et al., 2011). Examination of OPN is particularly timely, since it is notably upregulated during the inflammation associated with Alzheimer's disease (AD) and other neurodegenerative conditions (Choi et al., 2007; Comi et al., 2010; Kim et al., 2004; Wung et al., 2007).

The past century has seen substantial growth in our understanding of AD and the molecular mechanisms underlying its development. When detected within the brain, extracellular plaques, comprising predominantly of amyloid-β protein (Aβ), and intracellular neurofibrillary tangles, composed primarily of hyperphosphorylated tau, are still considered to be the pathological hallmarks of the disease (De Strooper and Karran, 2016; Glenner et al., 1984; Hardy et al., 1998). It has been shown that misfolded Aβ forms, especially aggregates of $A\beta_{40}$ and, moreover, $A\beta_{42}$ alloforms, are highly synaptotoxic and that their accumulation is pathognomonic to AD (Shankar et al., 2008). Furthermore, exploration of this disease in central nervous system tissues beyond the brain has revealed Aβ pathology in retinas of AD patients, including those at early stages (Koronyo et al., 2017; Koronyo-Hamaoui et al., 2011; La Morgia et al., 2016; Hart et al., 2016 #59).

Converging data from genetic, physiologic, biochemical, and clinical studies demonstrate a strong association between Aβ accumulation and neuroinflammation, synaptic loss, impaired neuronal function, and ultimately, debilitating cognitive decline (Selkoe, 2001 #73; Wyss-Coray, 2006). The progressive accumulation and aggregation of Aβ peptides in the brain are thought to result from an imbalance between their production and clearance (Mawuenyega et al., 2010; Saido, 1998). Inadequate cerebral $A\beta_{42}$ clearance was detected in sporadic common cases of AD (Mawuenyega et al., 2010). Moreover, the dramatic increase in cerebral Aβ begins as early as 20 years prior to symptom manifestation, far preceding clinical impairment (Bateman et al., 2012; Bilgel et al., 2016; Perrin et al., 2009). Therefore, a strategy capable of reducing Aβ levels in the brain, either by inhibiting production and the resulting aggregation or by promoting clearance, would be advantageous in preventing the development of AD.

Growing evidence suggests that infiltrating innate immune cells may play a key role in the clearance of cerebral Aβ plaques in murine models of AD (Bernstein et al., 2014; Butovsky et al., 2007; El Khoury et al., 2007; Koronyo et al., 2015; Koronyo-Hamaoui et al., 2009; Lai and McLaurin, 2012; Lebson et al., 2010; Malm et al., 2012; Simard et al., 2006). We are among a number of groups to demonstrate that immunomodulation can lead to increased cerebral infiltration by monocytes, cells directly involved in Aβ-plaque clearance. In our studies, we found that beneficial immunomodulation in double transgenic $APP_{SWE}/PS1_{\Delta E9}$ (ADtg) mice was facilitated either by altered myelin-derived antigens, such as glatiramer acetate (GA; also called Copaxone®) and MOG45D, or by adoptive transfer of inflammatory monocytes into the peripheral bloodstream (Bakalash et al., 2011; Bernstein et al., 2014; Butovsky et al., 2006, 2007; Frenkel et al., 2005; Koronyo et al., 2015; Koronyo-Hamaoui et al., 2009, 2011; Lebson et al., 2010). In particular, GA immunization alone and in combination with BM-$CD115^+$ monocyte (Mo^{BM}) blood enrichment delayed AD-like progression and profoundly attenuated various abnormalities associated with AD. Following therapy, we observed reduced levels of soluble and insoluble $A\beta_{42}$ in the brain, enhanced proteolytic degradation of Aβ (by MMP-9, ACE, neprilysin), regulation of neuroinflammation, and preservation of synapses and cognitive function in ADtg mice (Koronyo et al., 2015). In BM-derived macrophage ($M\Phi^{BM}$) cultures, GA activation increased phagocytosis of fibrillar Aβ, a change partly attributed to elevation of surface scavenger receptors (i.e. CD36, Scara-1) (Koronyo et al., 2015).

While the exact molecular mechanisms through which GA affects monocyte and macrophage recruitment and function in AD remain largely unclear, recent reports have suggested a promising link between a subset of these cells and neuroprotective clearance. Among these are the involvement of OPN-producing macrophages in the phagocytosis of fragmented cell debris following stroke (Shin et al., 2011), and an impairment of phagocytic activity in OPN-deficient mice (KO^{OPN}) (Schack et al., 2009; Toyonaga et al., 2015). These findings prompted us to investigate how cerebral OPN expression is impacted following GA immunomodulation in ADtg mice and how it relates to monocyte migration and Aβ-plaque burden. Furthermore, we have examined how OPN inhibition affects the immune phenotype of macrophages and its effect on their ability to phagocytose pathogenic $A\beta_{40}$ and $A\beta_{42}$ aggregates associated with AD.

2. Materials and methods

2.1. Mice

Double transgenic mouse models of Alzheimer's disease (ADtg) from the B6Cg-Tg (APPswe, PSEN1E9) 85Dbo/J strains and their age-matched non-transgenic (WT) littermates were purchased from Jackson Laboratories (MMRC stock #34832-JAX|APP/PS1), then bred and maintained at Cedars-Sinai Medical Center. ADtg mice carrying the human transgene allow for detection of Aβ forms with anti-human Aβ antibodies. OPN knock-out (KO^{OPN}) mice from the B6.129S6 (Cg)-*Spp1*^{tm1Blh}/J strain (Jackson laboratories stock #004936|OPN KO) were used for in vitro experiments. For our studies, mice with ages spanning from 2 months to 24 months old were used. For all in vitro experiments, bone marrow was collected from young mice, aged 8–16 weeks. In addition, young C57BL/6-tg (UBC-GFP) 30 Scha/J donor mice, aged 8–10 weeks, were used for adoptive transfer of bone marrow-derived GFP^+ monocytes. These mice express enhanced green fluorescent protein (GFP) under direction of the human ubiquitin C promoter. All mice in this study had a C57BL/6 congenic background, with males and females in equal number and age-matched when applicable. All experiments were conducted and recorded by researchers blinded to mouse genotypes and/or treatment. This research was performed in accordance with Cedars-Sinai Medical Center Institutional Animal Care and Use Committee (IACUC) guidelines under an approved protocol and complied with the current United States applicable laws.

2.2. Human brain tissues

Postmortem brain sections from the frontal cortex of 2 neuropathologically confirmed AD patients and 2 age- and gender-matched (cognitively normal) control individuals were prepared and analyzed by immunohistochemistry. Human tissues were obtained from the Alzheimer's Disease Research Center (ADRC) Neuropathology Core (IRB protocol: HS-042071) at the University of Southern California's (USC; Los Angeles, CA) Department of Pathology.

2.3. Glatiramer acetate (GA) immunization

Symptomatic 10-month-old ADtg male mice received either subcutaneous injections of 100 μg GA (also known as Copaxone, in 200 μl PBS; TEVA Neuroscience) or PBS alone (control). Injections were administered twice during the first week, then once a week for 8 weeks. After completing treatment, all mice were anaesthetized and perfused with ice-cold PBS supplemented with 0.5 mM EDTA. Brains were collected and analyzed or fixed in 2.5% paraformaldehyde (Sigma-Aldrich), and cryo-protected in 30% sucrose for further histological analysis.

Flow cytometry analysis was conducted on blood and brain of adult ADtg and WT mice (~3 month old; n = 4 mice/per group and genotype) that were immunized with GA or PBS, according to a regimen of twice a week the first 2 weeks then once a week the following 2 weeks (total of 6 injections). Blood (up to 0.5% of mouse body weight) was collected from the saphenous vein before and after the last GA injection. At the end of the experiment, all mice were perfused and brains were collected and immediately processed for flow cytometry analysis (n = 3 ADtg mouse brains per treatment group).

2.4. Adoptive transfer

$CD115^+$ monocytes from donor mice were isolated as previously reported in Koronyo et al. (2015). In short, after euthanasia, bone marrow cells were harvested from femurs, tibiae, and humeri, and enriched for mononuclear cells on a Ficoll-Paque PLUS (GE Healthcare) density gradient. The $CD115^+$ monocyte population was isolated with a MACS enrichment column using the biotinylated anti-CD115 mAb clone AFS98 (eBioscience) and streptavidin-coupled magnetic beads (Miltenyi Biotec), per manufacturer's protocols. After this procedure, the entire $CD115^+$ monocyte population ($5–6 \times 10^6$ cells/mouse) was injected into tail veins of 10-month-old ADtg mice once a month for 2 months.

2.5. Immunohistochemistry (IHC)

Coronal brain sections (30 μm thick) were treated for 30 min in antigen-retrieval solution (Dako) prior to serum-free protein blocking (Dako Cytomation). Sections were then hybridized with various primary antibodies (overnight at 4 °C): goat polyclonal OPN (R&D systems), mouse anti-human Aβ [residues 17–24, mAb clone 4G8 (1:100; Covance), and residues 1–16, mAb clone 6E10 (1:100; Covance)], rabbit anti-GFAP pAb (1:100; Sigma-Aldrich), rabbit anti-Iba1 pAb (1:250; Wako Chemicals), rabbit anti-GFP pAb (1:500; MBL), rat anti-CD68 mAb (1:100; Abcam), rabbit anti-iNOS pAb (1:100; Cell signaling), rat anti-CD45 mAb clone 30-F11 (1:25; BD Pharmingen), mouse anti-human CD45 mAb (1:20; BD Pharmingen), mouse anti-Tuj1 mAb (1:200; Abcam), rabbit anti-NeuN mAb (1:200; Abcam) and goat anti-MMP9 pAb (1:100; R&D systems). Hybridization with primary antibodies was followed by incubation with biotinylated secondary antibody and conjugation with horseradish peroxidase (HRP) [Vectastain Elite ABC kit from Vector laboratories using DAB-plus substrate chromogen system (DAKO)] or fluorophore-conjugated secondary antibodies (1 h at 37 °C; donkey anti-mouse, anti-rat, anti-goat, and anti-rabbit; 1:200; Jackson Immuno Research Laboratories) conjugated with Cy2, Cy3, and Cy5. Sections were mounted using ProLong Gold with DAPI (Molecular Probes, Life Technologies). Negative controls were processed using the same protocol with the omission of the primary antibody to assess non-specific labeling. A Carl Zeiss Axio Imager Z1 fluorescence microscope equipped with ApoTome (Carl Zeiss MicroImaging, Inc.) was used for microscopic analysis. AxioVision (release 4.6.3) software (Carl Zeiss) was used to process and analyze the images.

2.6. Thioflavin-S staining and CAA scores

For amyloid burden assessment in mouse/human brain parenchyma and vasculature, sections were stained with Thioflavin S (Thio-S, 1% w/v in 70% ethanol; Sigma-Aldrich) for 10 min at room temperature following the secondary antibody step, according to a previously described standard protocol (Koronyo et al., 2015). Various degrees of cerebral amyloid angiopathy (CAA) in animals were defined by analyzing Thio-S-labeled brain sections using a scale of 0–4 (0 indicates no CAA, 4 indicates severe CAA; 5 brain sections per animal), as previously described (Wyss-Coray et al., 2001).

2.7. Primary cultures of bone marrow-derived macrophages

Bone marrow-derived macrophages ($M\Phi^{BM}$) from WT or KO^{OPN} mice were generated from femurs and tibiae after euthanasia, and cultured for 6–7 days in complete RPMI 1640 medium (Life Technologies) supplemented with 10% FBS, 100 U/ml penicillin, 100 μg/ml streptomycin, 2 mM L-glutamine and 20 ng/ml MCSF (PeproTech). Primary cultures of $M\Phi^{BM}$ were then plated overnight with 1×10^5 cells per well (3–5 wells per condition) in 24-well tissue culture plates on glass coverslips. Next, macrophages were treated with either 30 μg/mL GA, 50 ng/ml Recombinant Human Osteopontin (rOPN; Peprotech), Brefeldin A (BFA; Sigma, 1X), or 10 μM Minocycline (Sigma) for a duration of 3 or 24 h (each component diluted in the culture medium). The control group was not treated. Immediately following addition of preformed fibrillar $A\beta_{1-42}$ or $A\beta_{1-40}$ (100 nM), plates were briefly centrifuged and incubated at 37 °C for 30 or 60 min. Cells were then rinsed with culture medium to remove non-incorporated Aβ, washed with PBS, and fixed in cold methanol (99.8%, −20 °C) for immunocytochemistry.

2.8. Immunocytochemistry (ICC)

After serum-free protein blocking (Dako Cytomation), cells were hybridized with various primary antibodies (overnight at 4 °C), including goat polyclonal OPN (R&D systems), mouse anti-human residues 1–16, mAb clone 6E10 (1:100; Covance)], rabbit anti-Iba1 pAb (1:250; Wako Chemicals), rat anti-CD68 mAb (1:100; Abcam), rabbit anti-iNOS pAb (1:100; Cell signaling), goat anti-MMP9 pAb (1:100; R&D systems), Rat anti-CD36 mAb (1:xx; Abcam), rabbit anti-LC3 pAb (1:250; Novus), mouse anti-Golgi mAb (1:50; Sigma-Aldrich), rabbit anti-EEA1 pAb (1:100; Millipore), rabbit anti-Rab7 mAb (1:100; Abcam), rat anti-SCARA1 mAb (1:100; AbD Serotec), and anti IL-10 pAb (1:100; R&D system). Hybridization with primary antibodies was followed by incubation with appropriate secondary polyclonal antibodies (1 h at 37 °C; donkey anti-mouse, anti-rat, anti-goat, and anti-rabbit; 1:200; Jackson Immuno Research Laboratories) conjugated with Cy2, Cy3, and Cy5. Sections were mounted using ProLong Gold with DAPI (Molecular Probes, Life Technologies) and analyzed as previously described.

2.9. Microscopy and quantification

Fluorescence of specific signals was captured with a Carl Zeiss Axio Imager Z1 fluorescence microscope equipped with ApoTome (Carl Zeiss MicroImaging, Inc.) using the same exposure time for each image. Images were analyzed using ImageJ software (NIH), converted to grayscale and using the same post-acquisition threshold for analysis. Manual counting of $OPN^+/CD45^{hi}$ and $Iba1^+/CD45^{hi}$ cells was performed with ImageJ software, using the 'analyze' grid, by analyzers blinded to mouse genotype and treatment groups. Quantification of the number and area (μm^2) of OPN^+ cells, $Iba1^+$-$CD45^{hi}$ and OPN^+CD45^{high} cells, $6E10^+$, Thio-S^+ and $4G8^+$ Aβ plaques, as well as OPN, iNOS, CD36, SCARA-1, IL10, and MMP9 immunoreactive area, were determined as follows: 1. For IHC, four to six coronal brain sections at 150-μm intervals per mouse were examined over an area covering both hippocampal and cortical regions (including entorhinal and cingulate cortex); 2. For ICC, five to ten images from each well (n = 3–6 wells per group), covering on average 100 cells per image, were analyzed.

2.10. Enzyme-linked immunosorbent assay (ELISA) on cell samples and brain homogenates

$M\Phi^{BM}$ cells in each well were lifted by 2 mM EDTA-PBS, collected in tubes, and centrifuged separating cells from supernatant. Cell pellets were lysed and re-suspended in a cocktail of RIPA buffer supplemented with 1% protease inhibitors (Thermo Scientific), and stored at −80 °C until use. Brain tissues, freshly collected after perfusion, were immediately and thoroughly homogenized in PBS buffer with 0.5% Triton X-100 (Sigma) and 1X protease inhibitor cocktail set I (Calbiochem), then processed as previously described (Koronyo et al., 2015).

After determination of protein concentration using the Pierce BCA Protein Assay Kit (Thermo Scientific), concentrations of $A\beta_{42}$, $A\beta_{40}$ and OPN were analyzed with an anti-human $A\beta_{1-42}$ and $A\beta_{1-40}$ specific sandwich ELISA kit (Invitrogen) and an anti-mouse OPN quantikine ELISA kit (R&D Systems), per manufacturer's instructions. The optical density of each well was read at 450 nm (with 540 nm correction for OPN) using the same microplate reader (Spectra Max 384 plus, Molecular Devices).

2.11. Western blotting

$M\Phi^{BM}$ were lifted from each cell by 2 mM EDTA-PBS, collected in an Eppendorf tube, and centrifuged. Cell pellets were lysed in RIPA buffer (Thermo Scientific) and supplemented with a cocktail of protease inhibitors (Thermo Scientific). Protein concentration was determined using a BCA Protein Assay Kit (Thermo Scientific). Aliquots of protein samples were electrophoretically separated using 4–12% Bis-Tris gels (Invitrogen), then transferred to nitrocellulose membranes, blocked in Tris-buffered saline (TBS) containing 5% (w/v) non-fat dry milk, and hybridized with appropriate primary antibodies, including rabbit anti-OPN pAb (Abcam), goat anti-OPN pAb (R&D systems), and β-Actin (Abcam). Rabbit anti-OPN pAb recognizes the full-length as well as the MMP-cleaved OPN fragments, whereas the goat anti-OPN pAb recognizes and provides a strong signal only for the full-length OPN. Membranes were then incubated with the appropriate HRP-conjugated secondary antibody prior to development with chemiluminescent substrates. Densitometric analysis of blots was conducted using ImageJ software, and each experimental sample was normalized to β-Actin.

2.12. Preparation of $A\beta_{42}$ and $A\beta_{40}$ fibrils

Lyophilized $A\beta_{1-40}$ and $A\beta_{1-42}$ peptides (Anaspec) were dissolved in ice cold hexafluoroisopropanol (HFIP) (Sigma) to create a monomeric solution of 100 μM. The HFIP was evaporated in a sterile hood creating a desiccated aggregate-free peptide film that can be stored at −20 °C. HFIP was used to ensure preparation of Aβ fibrils from uniform monomeric Aβ peptide layer. Leftover traces were removed in a SpeedVac for 2 h. To initiate fibril formation, Aβ films were resuspended in a sterile mixture containing 45% 20 mM $NaH_2PO_4 + Na_2HPO_4$ (pH 7.4) and 10% NaOH 60 mM in 45% H_2O, vortexed for 30 s. Aβ solutions were incubated on a shaker for 2 weeks at 37 °C. Pre-formed Aβ fibrils were then sonicated for 60 s and diluted to 100 nM in culture media prior to the phagocytosis assay.

2.13. OPN knockdown by siRNA in vitro

We used a set of three Stealth OPN siRNAs made up of 25-bp duplex oligoribonucleotides each, with sequences corresponding to the sense and antisense strands of OPN (Invitrogen). Equal amounts (100 nM each) of siRNAs were mixed and diluted in Opti-MEM (Gibco) to a final concentration of 100 nmol/L, then transiently transfected into $M\Phi^{BM}$ using Lipofectamine® RNAiMAX Transfection Reagent (Invitrogen), per manufacturer's protocol. Control macrophages were transfected with Stealth RNAi™ siRNA Negative Control. $M\Phi^{BM}$ were incubated for 48 h after transfection, and were used for subsequent experiments.

2.14. Cell length measurement

The long and short axes of cells were manually measured in μm from microscopic images (McWhorter et al., 2013) using length tools in the Axiovision Rel. 4.8 software package. At least 100 cells were examined in each experiment where individual cells were assayed by microscopy.

2.15. Flow cytometry analysis of murine peripheral blood

Blood collected into EDTA tubes was processed for flow cytometry analysis as follows.

After centrifugation (1800 RPM, 4 °C, 12 min), RBC lysis (1×; #420301, Biolegend) was applied on the cell pellets (2 ml of RBC lysis to 100 ul of whole blood, incubated for 13 min in dark and R.T.). After centrifugation (1800 RPM, 4 C°,5 min) and washes with FACS buffer (2% BSA, 0.1% w/v NaN_3, #438456, Sigma, in PBS), cells were counted in the presence of Trypan blue stain (0.4%; #15250-061, Gibco). Subsequently, cells were blocked with FC receptor blocking (anti mouse CD16/32, #101301), and stained for cell surface markers with the following antibodies: FITC-conjugated anti mouse-CD11b (clone M1/70; #101206), APC-conjugated anti-mouse CD115 (clone AFS98; #135510) and Pacific blue-conjugated anti-mouse Ly6C (clone H.K1.4; #128013). All required controls were added to the flow cytometry analysis including isotype control antibodies: Rat IgG2b, κ – FITC (clone RTK4530; #400605); Rat IgG2a, κ – APC (clone RTK2758; #400511); Rat IgG2c, κ – Pacific Blue™ (clone RTK4174; #400717) and Goat IgG – PE (clone Poly24030; #403004). All antibodies were diluted 1:100 and purchased from BioLegend.

After staining (30 min in dark, 4 °C), the cells were washed and centrifuged. Next, cells were fixed with 500 ul cold 2.5% PFA in PBS for 15 min in R.T., then washed and centrifuged twice. After fixation, cells were permeabilized with 2 ml Saponin buffer (0.1% w/v Saponin #S4521, Sigma, 0.05% w/v NaN_3, #438456, Sigma, in Hank's Balanced salt solution sterile 1x, Corning) for 5 min. Samples were centrifuged and cells were stained for intracellular markers with the following antibody: PE-conjugated anti-mouse OPN (#IC808P, R&D). After staining (30 min in dark, 4 °C), cells were washed and centrifuged twice, and PBS (1x, 300 ul) was finally added to the samples. Samples were analyzed with flow cytometer (BD LSRFoortessa™, BD Biosciences) and data were analyzed with FlowJo software (Tree Star, Inc.).

2.16. Flow cytometry analysis of myelomonocytes in ADtg mouse brain tissue

Whole brains freshly collected after perfusions were mechanically minced in a 70-μm cell strainer (Falcon; Corning Inc.) with ice-cold 2% fetal bovine serum (Atlanta Biological) in PBS. After centrifugation, homogenization and washing, pellets were suspended in 40% sterile Percoll (GE Healthcare) and centrifuged (850*g*, 4 °C, 25 min, without brake). Cell pellets were re-suspended in 70% sterile Percoll and centrifuged (800*g*, 4 °C, 20 min, without brake). Cells located in the top layer after the Percoll gradient were collected and washed. Mononuclear cells were counted in the presence of Trypan blue stain (0.4%; #15250-061, Gibco). Subsequently, cells were blocked with FC receptor blocking, 1 μg per 10^6 cells (anti mouse CD16/32, #101301), and stained (30 min in the dark, 4 °C) for cell surface markers with the follow-

ing antibodies: FITC-conjugated anti-CD11b clone M1/70 (#101206); Pacific blue–conjugated anti mouse -Ly6C (clone H. K1.4; #128013); and PE/Cy7-conjugated anti–CD45.2 clone 104 (#109830). All antibodies were diluted 1:100, and purchased from BioLegend. All required controls were added to the flow cytometry analysis including isotype control antibodies as previously described. After staining (30 min in dark, 4 °C) the cells were washed and centrifuged. Following steps (PFA fixation, saponin permeabilization, OPN intracellular staining and analysis) are similar to the blood processing (see above).

2.17. Statistical analysis

Experimental data was analyzed using GraphPad Prism 6.01 (GraphPad Software). In cases where three or more groups were compared, two-way or one-way ANOVA was performed, followed by the Tukey's, Dunnett's, or Bonferroni's multiple comparison test of paired groups. Two-tailed unpaired Student's *t*-tests were used in two-group comparisons. The statistical association between two or more variables was determined by Pearson's correlation coefficient (*r*) test (GraphPad Prism). Pearson's *r* indicates direction and strength of the linear relationship between two variables. Results are shown as means ± standard errors of the mean (SEMs). Degree of significance between groups is represented as follows: $^{*}p < 0.05$, $^{**}p < 0.01$, $^{***}p < 0.001$, and $^{****}p < 0.0001$. A p-value lower than 0.05 was considered significant. All data analysis was led by blind examiner; code was revealed when analyses were concluded.

3. Results

3.1. Distinct patterns of cerebral OPN expression associated with Alzheimer's disease

To investigate cerebral OPN distribution in various brain regions and cell types, we initially analyzed brain regions associated with AD (Fig. 1A) in symptomatic 13-month-old male ADtg mice in comparison with age- and gender-matched wild-type (WT) non-Tg littermates. Immunohistochemistry (IHC) revealed pronounced OPN expression patterns in the hippocampus (HC), cingulate cortex (CC), and entorhinal cortex (EC) in ADtg mice within or near Aβ plaques (Fig. 1B, C). Similar patterns of OPN expression were observed in brains of ADtg mice with peroxidase labeling (Fig. 1C). OPN immunolabeling was largely undetectable in control WT mice (Fig. 1B). Next, we screened for the type of cells that express cerebral OPN in both ADtg and WT mice (Fig. 1D, E). In ADtg mice, OPN protein did not colocalize with markers of neurons (Tuj1, NeuN) or reactive astrocytes (GFAP) in CC and EC (Fig. 1D). While OPN did not appear in resting parenchymal Iba1^{+} myeloid cells in association with plaques in both WT and ADtg mice, activated Iba1^{+} microglia/macrophages clustering around amyloid plaques showed strong OPN expression (Fig. 1E). As expected, no such plaque-related cell clusters were found in WT mice. In brain regions not typically associated with AD (i.e. striatum), OPN immunostaining was predominantly confined to neurons in both ADtg and WT mice (Fig. S1). Analysis of cerebral OPN levels by quantitative ELISA showed protein levels increased 1.6–2.2 times in the brains of ADtg versus WT mice, in both 13- and 24-month-old mice, and increased 2–3 times with aging (13- vs. 24-month-old mice) in both genotypes ($p < 0.01 - 0.0001$).

To further explore OPN expression patterns in brains of AD patients, frontal cortices from four AD patients and two age- and gender-matched controls were immunostained and analyzed. In support of findings from murine models of AD (Fig. 1), patients showed a marked increase in cortical OPN expression in comparison with controls (Fig. S2A, B). OPN was located within and around Iba-1^{+} and/or CD45^{+} myelomonocytic cells (i.e. microglia, macrophages), predominantly surrounding Thio-S^{+} amyloid plaques (Fig. S2C–H). Overall, these results indicate that in brain regions affected by AD, OPN is selectively expressed by myeloid cells surrounding Aβ plaques.

3.2. Elevated expression of cerebral OPN following immunomodulation therapy is associated with reduced parenchymal and vascular Aβ burden

Previously, we demonstrated that GA immunization alone or in combination with monocyte blood enrichment attenuates disease progression, and that this effect is mediated by cerebral recruitment and modulation of myelomonocytic populations surrounding Aβ plaques in ADtg mice (Butovsky et al., 2006, 2007; Koronyo et al., 2015; Zuroff et al., 2017). Given that OPN is an immunomodulator highly expressed by myelomonocytic cells, we studied the effects of this approach on OPN cerebral expression (Figs. 2–4). To this end, we analyzed the levels of OPN in AD-associated brain regions of symptomatic (13-month-old male) ADtg mice following s.c. GA immunization (once a week for 2 months) or combined treatment of weekly s.c. GA plus monthly i.v. injections of BM-derived CD115^{+} monocytes to the peripheral blood (for 2 months; GA + Mo^{BM}) in comparison with OPN levels in ADtg mice that underwent i.v. PBS injection (once a month for 2 months; control group). Representative micrographs of coronal brain sections covering HC and CC regions reveal elevated OPN immunoreactivity along with reduced 6E10^{+}-Aβ plaque burden in GA- and GA + Mo^{BM}-immunized mice in comparison with PBS controls (Fig. 2A). Similar results were observed in EC (not shown).

Quantitative IHC indicated that while 6E10^{+}-Aβ plaque burden diminished in all AD-associated brain regions (HC, CC, EC) of GA-immunized groups (GA and GA + Mo^{BM}) in contrast to that of PBS controls (Fig. 2B), OPN expression increased, especially in cortical regions following combined GA + Mo^{BM} treatment (Figs. 2C and S3A). A quantitative ELISA analysis of OPN protein levels in brain homogenates confirmed that both treatment groups (GA, GA + Mo^{BM}) expressed significantly increased (1.4- and 2.1-fold) OPN compared with PBS control ADtg mice (Fig. 2D; $p < 0.001$). Further, to evaluate changes in OPN immunomodulator levels per inflammatory plaque lesion site, we next analyzed the ratio of OPN expression against area of 4G8^{+} or 6E10^{+} plaque burden (Fig. 2E and S3B, C). Specifically, the ratios of OPN-positive area to Aβ plaque area in EC, CC, HC and total brain regions were calculated. Data indicated greater increases in OPN expression (2.3- and 4.2-fold, respectively) in GA and GA + Mo^{BM} groups versus the PBS-control group (Fig. 2E; $p < 0.01 - 0.0001$). Notably, OPN expression in cortical regions (CC, EC) increased more substantially than in the hippocampus following GA immunization (Fig. S3B). This elevation of OPN levels within Aβ plaques following combined treatment (GA + Mo^{BM}) was consistently larger than that resulting from GA-immunization alone (Figs. 2E and S3C). To evaluate the relationship between OPN and Aβ levels in the brain, we analyzed paired parameters from individual mice using the Pearson's coefficient (*r*) correlation test (Figs. 2F–G and S3D–F). These analyses indicated a strong inverse relationship between OPN and Aβ plaque burden (Figs. 2F and S3D; Pearson $r = -0.65$, $p = 0.008$), especially in cortical regions. Furthermore, total OPN protein levels were inversely related to insoluble $A\beta_{42}$ (Fig. 2G; $r = -0.73$, $p = 0.017$) but not to soluble $A\beta_{42}$ (Fig. S3F). Together, these data demonstrate that upregulation of cerebral OPN by GA immunization, with or without monocyte blood enrichment, is concomitant with a reduction of parenchymal insoluble Aβ deposits in ADtg mice.

Cerebral amyloid angiopathy (CAA), a complex pathological feature found in most AD patients, involves vascular changes and cerebrovascular amyloid deposition (Ellis et al., 1996), where

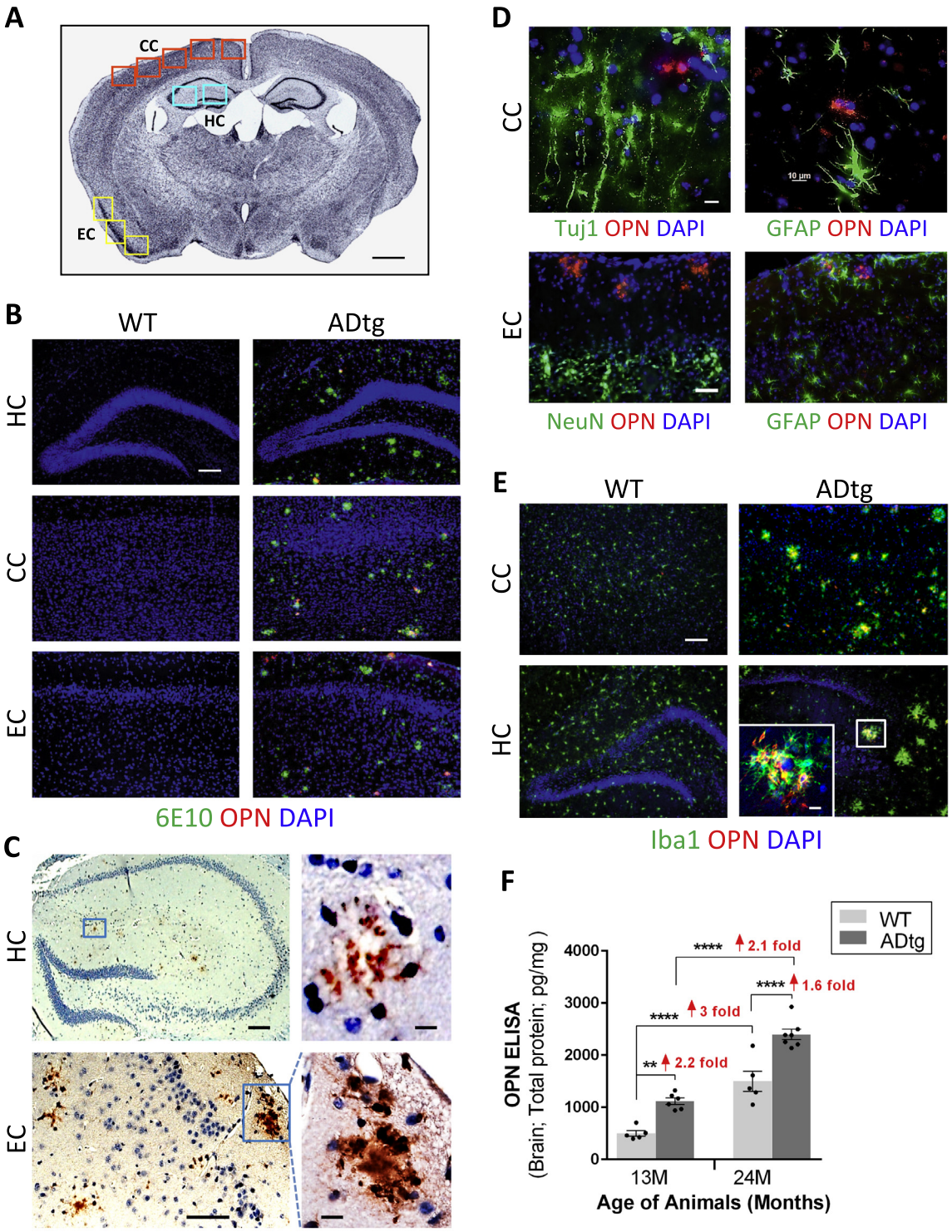

Fig. 1. OPN expression patterns in brains of ADtg and WT mice. (A) Quantification scheme for coronal brain sections. Representative Nissl-stained image of mouse brain at Bregma-2.65 mm. Scale bar: 1 mm. Cingulate cortex (CC), hippocampus (HC) and entorhinal cortex (EC) were included in subsequent quantitative analyses. (B) Representative fluorescent micrographs of brains from ADtg and age-matched WT mice, immunolabeled for anti-OPN (red), anti-human Aβ (6E10; green), and nuclei (DAPI, blue). OPN immunostaining was detected within and around Aβ plaques in ADtg mice in all AD-associated brain regions (HC, CC and EC). In WT animals, no Aβ or OPN immunolabeling was detected. (C) Photomicrographs of brain sections (HC and EC) from ADtg mice show OPN immunohistochemistry by labeling with horseradish peroxidase (HRP)-conjugated secondary antibody. OPN is abundant in layers II/III of EC and often forms plaque-like structures. (D) Representative fluorescent micrographs of ADtg mouse brain sections (CC and EC) display immunostaining for OPN (red) and neuronal markers, Tuj1 or NeuN, or the astrocyte marker, GFAP. (E) OPN (red) was expressed by a subset of Iba1^{+} cells (green) in ADtg mice but not in WT-mice. Scale bars: 100 μm, inserts: 10 μm. (F) Quantitative ELISA analysis of OPN levels in brain lysate from ADtg and WT littermate groups at 13 and 24 months of age (equal numbers of females and males). n = 5–6 mice per group. Fold changes indicated in red. Group means, SEMs and individual data points are shown. $^{**}p < 0.01$, $^{****}p < 0.0001$, by one-way ANOVA and Tukey's multiple comparisons post test.

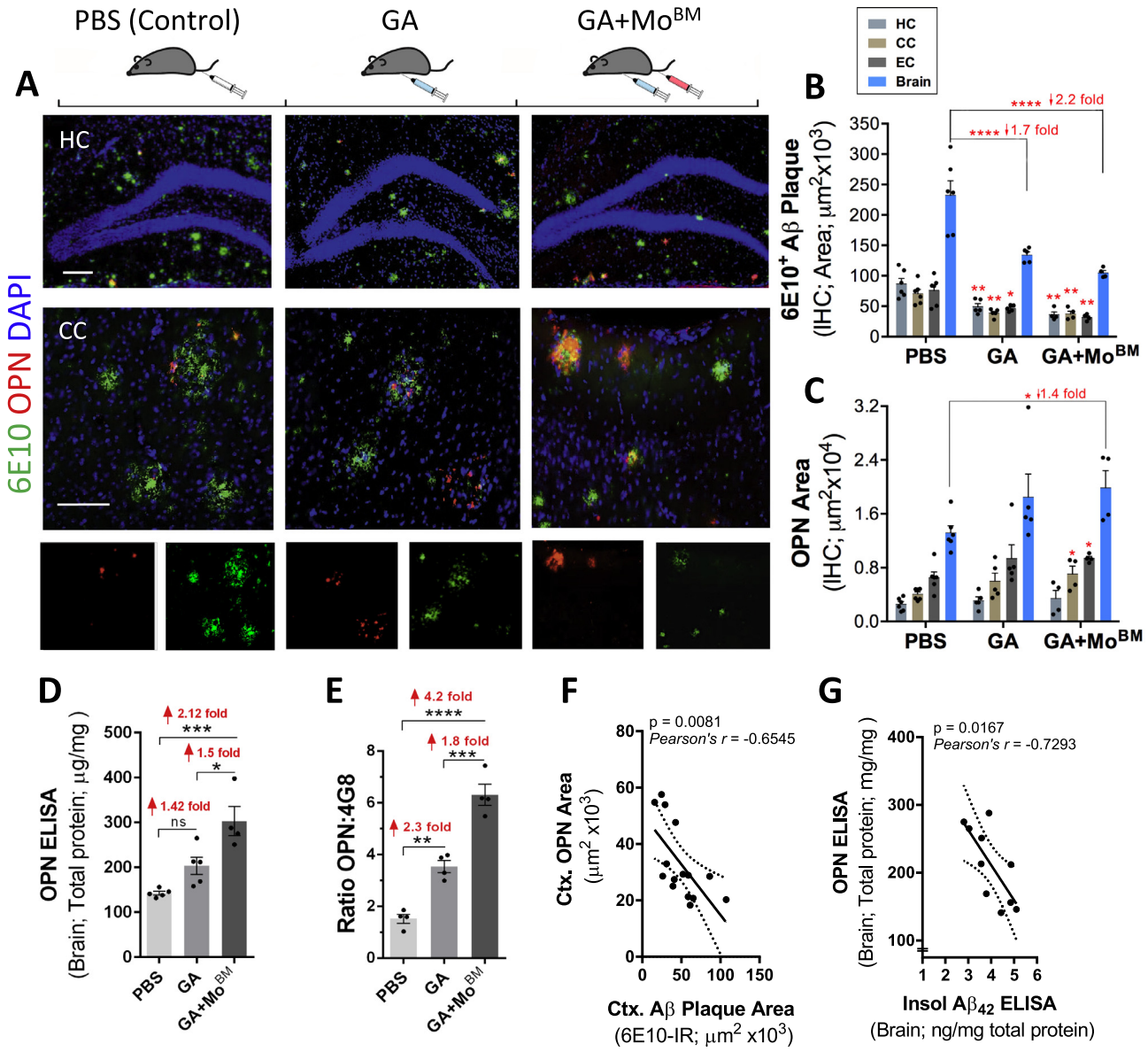

Fig. 2. Increased cerebral OPN expression associated with decreased Aβ plaque burden. (A) Fluorescent micrographs of coronal brain sections from HC (20× magnification, top panel) and CC (63×, lower panel) regions display OPN (red) and Aβ (6E10, green) aggregation patterns for all experimental ADtg mouse groups: s.c. GA immunization, GA + Mo^{BM} [GA s.c. immunization combined with i.v. adoptive transfer of bone marrow-derived $CD115^+$ monocytes (Mo^{BM})], and i.v. PBS injection as a control group (n = 4–6 male mice/group). Nuclei stained with DAPI. Lower row displays single channels of OPN (red) and $6E10^+$ (Aβ, green). Scale bars: 100 μm. (B, C) Quantitative IHC analyses of $6E10^+$-plaque area and OPN immunoreactive area in brains of ADtg mice (n = 4–6 mice/group). Data by region (HC, CC, and EC) accompanies total brain levels. (D) Quantitative ELISA analysis of OPN levels in brain lysates from all ADtg mouse groups (n = 4–5 mice/group). (E) Ratio between cerebral OPN^+ area and $4G8^+$-plaque area for all experimental groups (n = 4 mice/group). (F, G) Correlation analyses between cerebral OPN and Aβ burden: (F) Inverse correlation between cortical (Ctx.) OPN^+ area and $6E10^+$-Aβ plaque burden, and (G) inverse correlation between cerebral OPN and insoluble $Aβ_{42}$ levels (ELISA). Correlation analyses performed using Pearson's coefficient (r) test (n = 10–15 ADtg mice). Fold changes indicated in red. Group means, SEMs and individual data points are shown. $^*p < 0.05$, $^{**}p < 0.01$, $^{***}p < 0.001$, $^{****}p < 0.0001$, by one-way ANOVA and Tukey's or Dunnett's multiple comparisons post-tests (B–E) for comparison between experimental groups and PBS control or by two-tail unpaired Student's t-test for analysis between two groups (C).

$Aβ_{40}$ is the principal amyloid constituent (Herzig et al., 2006). We examined Aβ deposition in cerebral vessels by staining cortical and hippocampal brain regions with Thioflavin S (Thio-S) and further determined CAA severity scores (Fig. 3A, B), as previously described (Wyss-Coray et al., 2001). Results revealed that GA immunization significantly decreased vascular amyloid burden by 2.2 times (Fig. 3B; $p < 0.001$) as compared to PBS-treated ADtg mice. Combined treatment of GA immunization and Mo^{BM} also effectively cleared vascular Aβ deposits (Fig. 3B; 4.1-fold reduction, $p < 0.0001$). To determine the relationship between CAA severity and soluble/insoluble $Aβ_{40}$ and $Aβ_{42}$ alloforms, we performed multiple correlation analyses using the Pearson's coefficient (r) test (Fig. 3C–F). We found a highly significant direct association between CAA and levels of $Aβ_{40}$ peptide, both soluble and insoluble, in the brains of ADtg mice (Fig. 3C, D; $r > 0.76$, $p = 0.0001 – 0.0002$). While a positive correlation between CAA and insoluble $Aβ_{42}$ levels was observed (Fig. 3E), no such correlation was found with soluble $Aβ_{42}$ (Fig. 3F). We next analyzed the relationship between OPN and vascular-associated amyloid deposition (Fig. 3G–I), and found statistically significant evidence that cerebral OPN levels are inversely related to both vascular amyloid burden (Fig. 3G; $r = 0.72$, $p = 0.008$) and soluble/insoluble $Aβ_{40}$

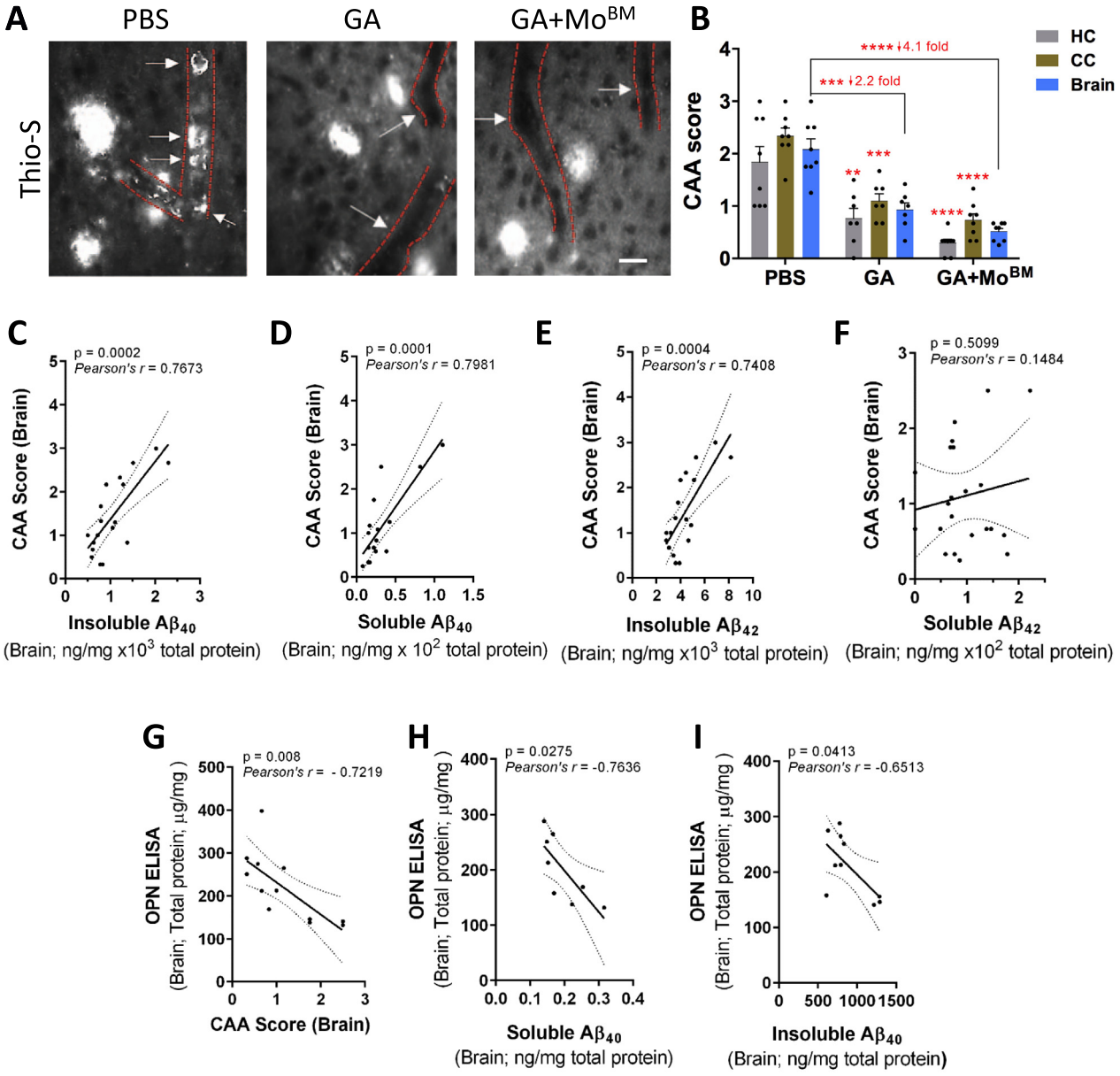

Fig. 3. Reduced cerebral vascular amyloid and $A\beta_{40}$ burden correlate with increased levels of cerebral OPN. (A) Representative photomicrographs show Thioflavin-S (Thio-S)$^+$ amyloid burden in brain parenchyma and vasculature; arrows and red delimitations indicate vascular Aβ deposits in respective cortical regions of GA-immunized (with and without grafted monocytes) vs. control (PBS-injected) ADtg mice. Thio-S staining revealed not only lesser parenchymal plaque burden in GA immunized groups but also reduction of vascular Aβ deposits. (B) Quantitative Thio-S$^+$ CAA score assessment by brain region (HC and CC) and average in ADtg mouse groups (n = 7–8 mice/group). (C–F) Correlation analyses reveal strong, significant linear correlations between vascular CAA burden and both (C) insoluble and (D) soluble $A\beta_{40}$ levels in the brain (ELISA) as well as with (E) cerebral insoluble $A\beta_{42}$, but no correlation with (F) soluble $A\beta_{42}$ levels (ELISA). (G–I) Inverse correlations between cerebral OPN levels and (G) CAA scores, (H) soluble $A\beta_{40}$, and (I) insoluble $A\beta_{40}$ in ADtg mouse brains (ELISA). Correlation analyses performed using Pearson's coefficient (r) test (n = 10–15 ADtg mice). Fold changes indicated in red. Group means, SEMs and individual data points are shown. $^{**}p < 0.01$, $^{***}p < 0.001$, $^{****}p < 0.0001$, by one-way ANOVA and Dunnett's multiple comparisons post-tests.

(Fig. 3H, I; $r > 0.65$, $p < 0.05$). Collectively, these results suggest that GA immunization, and to a greater degree its combination with monocyte blood enrichment, leads to an upregulation of cerebral OPN that is tightly associated with reduced vascular and parenchymal Aβ burden in ADtg mice.

3.3. OPN is predominantly expressed by infiltrating monocyte-derived macrophages involved in Aβ clearance

To identify OPN-expressing cells in ADtg mouse brains, we used two different approaches (Koronyo et al., 2015). To distinguish infiltrating monocytes/macrophages (Mo/MΦ) from microglia, we first used the combined Iba1 and CD45 markers (Fig. 4A). Fluorescent IHC analysis revealed that OPN is selectively expressed by infiltrating Iba1$^+$CD45^{high} Mo/MΦ in contrast to Iba1$^+$CD45$^{int\text{-}low}$ resident microglia (Fig. 4A, merged image; separate channels in Fig. 4A'). These infiltrating OPN-expressing Iba1$^+$CD45^{high} Mo/MΦ accumulated at and around plaque lesion sites, and the localization of Aβ within these cells (Fig. 4A, arrow; enlarged framed image in Fig. 4A") suggests their direct involvement in Aβ phagocytosis. Brain-infiltrating monocytes expressing OPN were also identified in GA + Mo^{BM}-treated ADtg mice through adoptive transfer of GFP-labeled BM-derived CD115$^+$-Mo into the peripheral blood (Fig. 4B). In EC, GFP$^+$CD45^{high} Mo/MΦ frequently

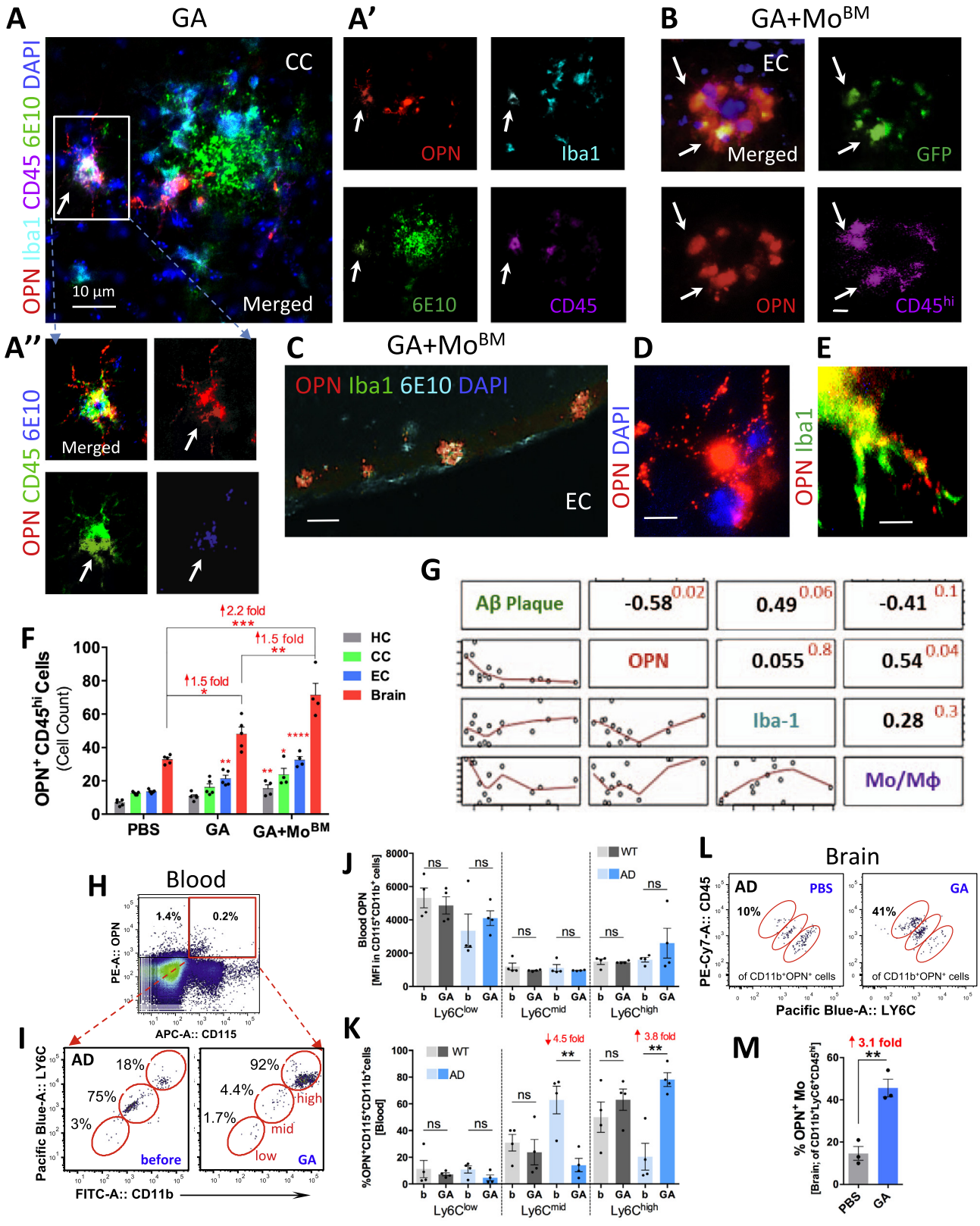
A
GA
OPN Iba1 CD45 6E10 DAPI
CC
10 µm
Merged
A'
OPN
Iba1
6E10
CD45
B
GA+Mo^BM
EC
Merged
GFP
OPN
CD45^hi
A''
OPN CD45 6E10
Merged
C
GA+Mo^BM
OPN Iba1 6E10 DAPI
EC
D
OPN DAPI
E
OPN Iba1
F
OPN+ CD45hi Cells (Cell Count)
2.2 fold
1.5 fold
1.5 fold
HC
CC
EC
Brain
PBS
GA
GA+Mo^BM
G
Aβ Plaque
-0.58 0.02
0.49 0.06
-0.41 0.1
OPN
0.055 0.8
0.54 0.04
Iba-1
0.28 0.3
Mo/Mϕ
H
Blood
1.4%
0.2%
PE-A:: OPN
APC-A:: CD115
I
AD
18%
75%
3%
before
92%
4.4%
1.7%
high
mid
low
GA
Pacific Blue-A:: LY6C
FITC-A:: CD11b
J
Blood OPN [MFI in CD115+CD11b+ cells]
WT
AD
ns
Ly6C^low
Ly6C^mid
Ly6C^high
K
%OPN+CD115+CD11b+cells [Blood]
4.5 fold
3.8 fold
L
Brain
AD
PBS
GA
10%
41%
of CD11b+OPN+ cells
PE-Cy7-A:: CD45
Pacific Blue-A:: LY6C
M
% OPN+ Mo [Brain; of CD11b+Ly6C+CD45hi]
3.1 fold
PBS
GA

expressed high levels of OPN, in contrast to resident microglia (GFP^{neg}-$CD45^{intermediate-low}$). Arrows indicate the localization of OPN in $GFP^{+}CD45^{high}$ Mo/MΦ in Fig. 4B. Notably, Mo/MΦ expressing high OPN were often located in EC and clustered at plaque lesion sites (Fig. 4C). We also examined the subcellular localization of OPN within infiltrating Mo/MΦ. OPN showed a punctate staining pattern in vesicular compartments and across the cell body and processes (Fig. 4D, E). OPN expression was particularly strong in the perinuclear subregion (Fig. 4D), apparently in the trans-Golgi network compartments (not shown; further in vitro examination below revealed OPN colocalization with a Golgi biomarker).

Next, we quantified $OPN^{+}CD45^{high}$ cells manually in AD-associated brain regions. Substantial 1.5- and 2.2-fold increases in number of infiltrating $OPN^{+}CD45^{high}$ cells, particularly in EC, were respectively detected in GA and GA + Mo^{BM} groups in contrast to PBS controls (Fig. 4F; $p < 0.01 - 0.0001$). Multifactor correlogram analyses confirmed that OPN expression inversely relates to Aβ plaque burden and associates directly with brain-infiltrating Mo/MΦ (Figs. 4G and S4A). Similarly, Pearson's correlation analysis demonstrated a significant direct linear relationship between cerebral OPN expression and recruited $Iba1^{+}CD45^{high}$ Mo/MΦ in ADtg mice (Fig. S4B; $r = 0.57$, $p = 0.025$). We further found a tighter association between expression of the OPN cytokine and brain-infiltrating $CD45^{hi}$ myeloid cells per plaque (Fig. S4C; $r < 0.61$, $p = 0.0001$).

Previously, we found that our immunomodulation approach altered the immunological environment in brains of ADtg mice, characterized by elevation of the Aβ-degrading enzyme matrix metalloproteinase (MMP)-9 (Bakalash et al., 2011; Butovsky et al., 2006; Koronyo et al., 2015; Koronyo-Hamaoui et al., 2009) as well as the chemokine monocyte chemoattractant protein-1 (MCP-1/CCL2), a key regulator of Mo/MΦ migration into the brain (El Khoury et al., 2007). We evaluated whether changes to these factors relate to cerebral OPN levels through Pearson (r) correlation analyses (Fig. S4D–G), and our data suggest strong positive associations between levels of OPN and MCP-1 (Fig. S4D; $r = 0.73$, $p < 0.03$), as well as between OPN area or protein levels and MMP-9 (Fig. S4E, F; $r = 0.62$, $p < 0.05$). Cortical OPN-expressing $CD45^{hi}$ Mo and MMP-9 protein levels also show a tight linear correlation (Fig. S4G; $r = 0.74$, $p = 0.0016$).

To assess how GA affects OPN expression in peripheral blood monocytes, an additional cohort of adult ADtg mice and age- and gender-matched WT littermates underwent flow cytometry analysis of peripheral blood before and after GA immunization (Figs. 4H–K and S5A–H). Immunolabeling of blood monocytes with several biomarkers (CD11b, CD115, and Ly6C) allowed detection of OPN-expressing monocyte subpopulations. $CD115^{+}$OPN-expressing monocytes represent a small ~0.2% population of murine blood cells (Fig. 4H, red box). In general, there were no significant differences in percentage of total blood cell population or mean OPN expression (MFI) in blood monocytes following GA immunization in both WT and ADtg mice (Fig. S5B, C). Further gating of $OPN^{+}CD115^{+}$ into three monocyte subpopulations, $CD11b^{+}$-$Ly6C^{low}$, $CD11b^{+}Ly6C^{medium}$, and $CD11b^{+}Ly6C^{high}$ showed no differences in MFI values before and after GA immunization in either genotype (Fig. 4J). However, significant differences in percentage of $CD11b^{+}Ly6C^{medium}$ and $Ly6C^{high}$ monocytes were detected after GA immunization in ADtg mice (Fig. 4K). Following GA immunization, a shift occurred in subpopulations of $CD115^{+}$-$CD11b^{+}Ly6C^{mid}$ and $CD115^{+}CD11b^{+}Ly6C^{high}$ monocytes, with the percentage of the former reducing 4.5 times and the latter inflammatory group growing 3.8 times in ADtg mice (Figs. 4K and S5D, E; $p < 0.01$). Examination of $CD115^{neg}CD11b^{+}$ cells that express OPN and exhibit $Ly6C^{low}$, $Ly6C^{medium}$, or $Ly6C^{high}$ (Fig. S5F) in WT and ADtg mice indicated that GA immunization did not affect these populations in the blood (Fig. S5G, H). While our data indicate no change to average OPN expression in blood monocytes, they do demonstrate an increase in the OPN-expressing inflammatory $CD115^{+}CD11b^{+}Ly6C^{high}$ monocyte subpopulation following GA immunization, specific to ADtg mice.

We have previously (Koronyo et al., 2015) and above (Fig. 4A–F) demonstrated that the inflammatory monocyte subpopulation increasingly infiltrates the brain parenchyma and migrates to amyloid plaque sites in GA-immunized ADtg mice. Flow cytometry analysis of infiltrating OPN-expressing monocytic cells ($CD11b^{+}$-$Ly6C^{+}CD45^{high}$; Figs. 4L and S5I) in brain tissues of ADtg mice ($n = 6$ mice) indicated a significant 3.1-fold increase in their percentage in the brains of GA-immunized as compared to PBS-injected mice (Fig. 4M; $p < 0.01$). Collectively, we report that GA immunomodulation, with and without monocytes, increases brain-recruitment of OPN-expressing Mo/MΦ tightly associated with Aβ-plaque clearance in ADtg mice.

3.4. OPN expression patterns in primary cultures of BM-derived macrophages

To investigate how OPN impacts macrophage phenotype and its role in macrophage-mediated Aβ phagocytosis and degradation, we further studied OPN loss- vs. gain-of-function in BM-derived MΦ exposed to pathological forms of Aβ. The in vitro experimental

Fig. 4. Selective expression of OPN by blood monocytes and brain-infiltrating monocyte/macrophages involved in Aβ uptake following GA immunization. (A–E) Fluorescent micrographs of cortical regions of GA-immunized ADtg mice, with and without grafted GFP^{+}-Mo^{BM} (GA + Mo^{BM}). Scale bars: 10 μm unless otherwise indicated. (A) Infiltrating Mo/MΦ identified by combined $Iba1^{+}$ and $CD45^{high}$ immunolabeling in GA-immunized mouse brains. Cerebral OPN, Aβ (6E10) and nuclei (DAPI) also shown. (A') Images of separate channels; arrow indicates an infiltrating OPN-expressing $Iba1^{+}CD45^{high}$ MΦ engulfing Aβ. (A") Region of interest in box above illustrates the colocalization of Aβ (6E10) with OPN-positive $Iba1^{+}CD45^{high}$ MΦ. (B) Brain-infiltrating monocytes expressing OPN were also identified in GA + Mo^{BM}-treated mice through a second approach: adoptive transfer of a GFP-labeled BM-derived $CD115^{+}$-monocyte subset injected into the tail vein of symptomatic ADtg mice. In EC, $GFP^{+}CD45^{high}$ Mo/MΦ expressed OPN abundantly, in a manner distinct from resident microglia (GFP^{neg}-$CD45^{intermediate-low}$). Arrows indicate colocalization of OPN and $GFP^{+}CD45^{high}$ Mo/MΦ. (C) OPN-expressing $Iba1^{+}$ myelomonocytic cells were associated with plaques, especially at the border of EC. Scale bar = 50 μm. (D, E) Puncta staining patterns of subcellular OPN in vesicular compartments across cell body and along $Iba1^{+}$ processes, with particularly intense signal in the perinuclear subregion. (F) $OPN^{+}CD45^{high}$ cell count in HC, CC, EC and combined brain regions ($n = 4$–5 ADtg mice/group). Fold increases relative to PBS controls or GA-treated group indicated in red. (G) Quantitative multifactor correlogram analysis (Pearson's test) demonstrated significant linear association between OPN and monocyte infiltration in ADtg mice, and inverse relations to Aβ plaque burden ($n = 15$ mice). (H–K) Flow cytometry analysis on blood monocytes isolated from additional cohort of adult ADtg and age- and gender-matched WT littermates before and after GA immunization ($n = 4$ mice/genotype). (H) Initial gating of CD115-positive cells expressing OPN in red box. (I) OPN^{+} CD115-positive blood monocyte subpopulation in red box further analyzed by flow cytometry using monocyte biomarkers CD11b and Ly6C. (J, K) The OPN-expressing $CD11b^{+}CD115^{+}Ly6C$ monocyte subpopulation in the blood was gated into three groups, $Ly6C^{low}$, $Ly6C^{mid}$ and $Ly6C^{high}$, showing differences in percentage of total cells before and after GA immunization in ADtg mice. Quantitative analysis of (J) mean fluorescence intensity (MFI) values and (K) proportions of cells in percentage before (b) and after immunization (GA). (L, M) Flow cytometry analysis on myelomonocytes isolated from perfused brains of GA-immunized vs. PBS-injected ADtg mice ($n = 3$ mice/group). (L) Final gating of $OPN^{+}CD11b^{+}$ myelomonocytes in the brain into three populations of $Ly6C^{+}CD45^{hi}$, $Ly6C^{+}CD45^{mid}$ and $Ly6C^{+}CD45^{low}$ (shown in red ellipses). (M) Percentage of $OPN^{+}CD11b^{+}$ $Ly6C^{+}CD45^{hi}$ infiltrating monocytes in the brain of GA vs. PBS control ADtg mice. Group means, SEMs and individual data points are shown. NS, no statistical significance. $^{*}p < 0.05$, $^{**}p < 0.01$, $^{***}p < 0.001$, $^{****}p < 0.0001$, by one-way (F) or two-way (J–K) ANOVA followed by Dunnett's or Bonferroni's multiple comparisons post tests or two-tail unpaired Student's t-test (M).

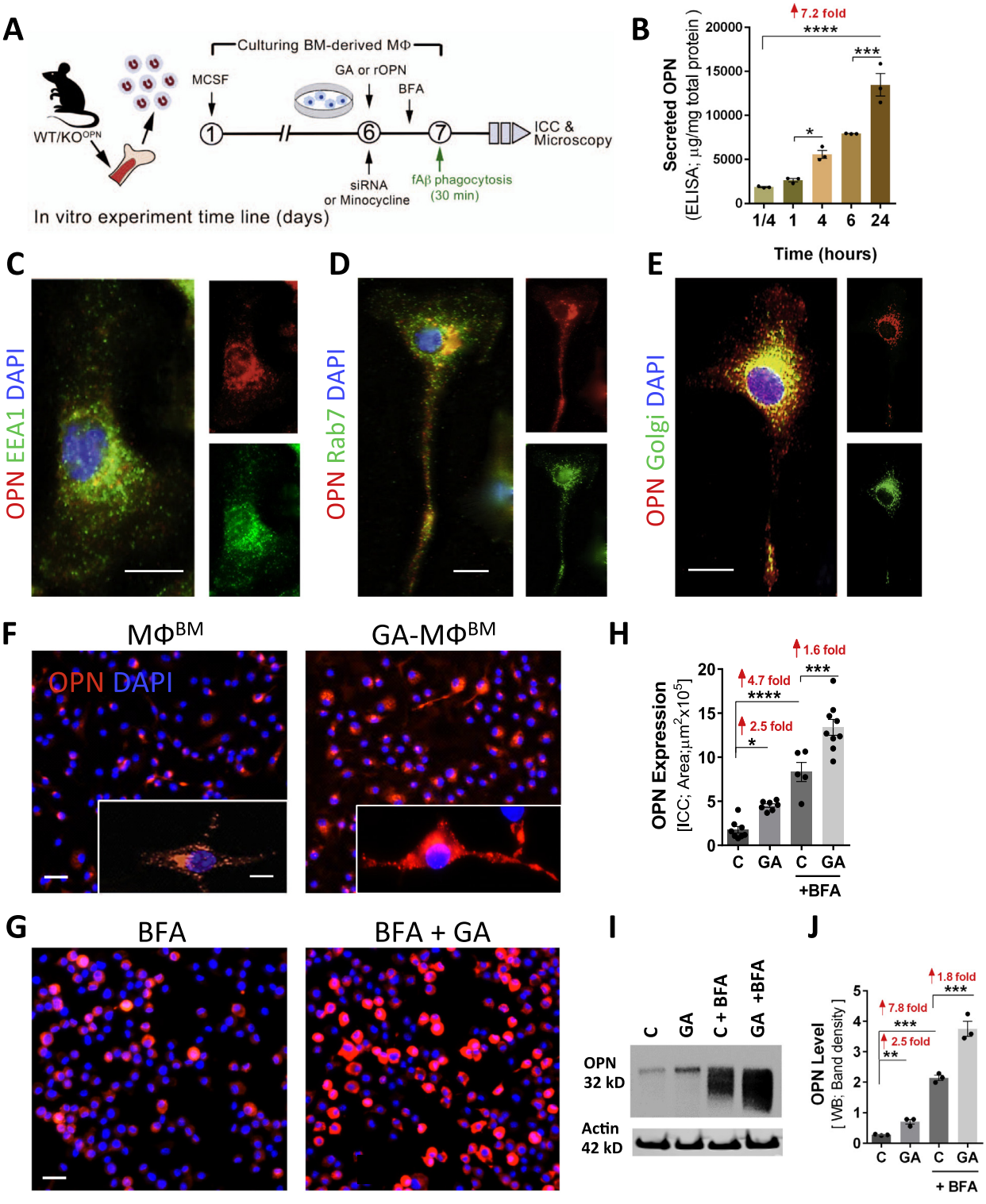
A
Culturing BM-derived MΦ
MCSF
GA or rOPN
BFA
WT/KOOPN
ICC & Microscopy
siRNA or Minocycline
fAβ phagocytosis (30 min)
In vitro experiment time line (days)
B
7.2 fold
Secreted OPN (ELISA; µg/mg total protein)
Time (hours)
C
OPN EEA1 DAPI
D
OPN Rab7 DAPI
E
OPN Golgi DAPI
F
MΦBM
GA-MΦBM
OPN DAPI
H
OPN Expression [ICC; Area;µm2x10-5]
1.6 fold
4.7 fold
2.5 fold
C GA C GA
+BFA
G
BFA
BFA + GA
I
C GA C + BFA GA +BFA
OPN 32 kD
Actin 42 kD
J
OPN Level [WB; Band density]
1.8 fold
7.8 fold
2.5 fold
C GA C GA
+ BFA

paradigm included isolation of BM from young WT or OPN-null ($OPN^{-/-}$ knockout; hereafter referred to as KO^{OPN}) donor mice, their differentiation into mature macrophages ($M\Phi^{BM}$), and a series of experiments involving treatments such as GA (GA-$M\Phi^{BM}$), recombinant OPN (rOPN), and/or siRNA inhibition, followed by a 30-min exposure to $A\beta_{40}$ and $A\beta_{42}$ fibrils (Fig. 5A). We initially explored secretion patterns of the cytokine OPN in $M\Phi^{BM}$ media over the course of 24 h (Fig. 5B). Our analysis suggests that OPN is constitutively expressed and secreted to the extracellular space by $M\Phi^{BM}$, is detectable even at the 15-min time point, and accumulates in substantial amounts over a full-day period (Fig. 5B; 7.2-fold increase, $p < 0.0001$). Next, we examined the patterns of intracellular OPN expression in $M\Phi^{BM}$ using various antibodies recognizing subcellular biomarkers (Figs. 5C–E and S6A). In $M\Phi^{BM}$ cultures, OPN often displayed intense perinuclear immunolabeling and punctate patterns across the cell body and processes, suggesting that OPN was located in transport vesicles (Fig. 5C–E). OPN did not typically colocalize with early endosomes (early endosomal antigen EEA1/Rab5a; Fig. 5C), late endosome/lysosomes (Ras-related protein Rab7; Fig. 5D), or autophagosomes (light chain 3 protein LC3; Fig. S6A): biomarkers representing internalization/uptake vesicles fated for intracellular degradation. However, OPN was mostly localized within the Golgi apparatus, part of a major secretory pathway, as detected via the anti-Golgi marker 58K protein antibody (Fig. 5E), implying that the cytokine is constantly expressed and sorted through the trans-Golgi network (TGN) for post-translation modifications prior to secretion.

We subsequently assessed the impact of GA pretreatment on OPN expression in $M\Phi^{BM}$ cultures in the absence of Aβ fibrils (Figs. 5F–J and S6B). This revealed that GA significantly induced OPN expression in $M\Phi^{BM}$, mirroring our in vivo results, and further increased when TGN-derived secretion vesicles were inhibited by Brefeldin A (BFA; Fig. 5F vs. G) (Rosa et al., 1992). While $M\Phi^{BM}$ without BFA showed typical elongated morphology and a punctate/vesicular OPN signal (Fig. 5F, inserts), $M\Phi^{BM}$ undergoing BFA blockage of TGN-derived protein secretion showed decreased cell adhesion with a rounded morphology, and newly-synthetized OPN trapped within (Fig. 5G). The BFA condition showed substantial accumulation of OPN in $M\Phi^{BM}$ in short periods of time (i.e. within 1-3 h). Quantitative immunocytochemistry (qICC) confirmed significant 1.6- and 2.5-fold increases in OPN production/expression (with and without BFA, respectively) in GA-$M\Phi^{BM}$ vs. untreated $M\Phi^{BM}$ (Fig. 5H). A quantitative ELISA analysis and Western blot assessments of OPN in cell lysates validated that regardless of BFA condition, GA markedly increased OPN expression and production 1.4–2.5 times in $M\Phi^{BM}$ (Figs. 5I,J and S6B; $p < 0.01 - 0.001$). Taken together, our data indicate that the immunomodulator OPN is constitutively expressed and secreted by $M\Phi^{BM}$ and that GA substantially increases its levels.

3.5. Phagocytosis of fibrillar Aβ is OPN dependent

To study whether OPN gain-of-function induces $M\Phi^{BM}$ phagocytosis of pathogenic Aβ aggregates, we first examined whether increased OPN expression via GA is associated with improved phagocytosis of $A\beta_{40}$ and $A\beta_{42}$ fibrils. Representative high-magnification Z-stack images demonstrate that intracellular OPN expression in $M\Phi^{BM}$ is accompanied by phagocytosis of fibrillar (f)$A\beta_{42}$ (Fig. 6A). $M\Phi^{BM}$ were then pretreated with GA (30 μg/mL, overnight) and exposed to $fA\beta_{42}$ for 30 min. Enhanced $fA\beta_{42}$ uptake was associated with increased OPN expression in GA-$M\Phi^{BM}$ when compared with untreated $M\Phi^{BM}$ (Fig. 6C vs. B). Representative images show a distinct pattern of OPN immunoreactivity within somas and along processes of $CD68^+$ (a phagocytic macrophage marker) phagocytes, with strong perinuclear and evenly distributed vesicular signals, accompanied by separated punctate Aβ labeling. This staining was substantially intensified after GA treatment (Fig. 6A–C). Exposure of $M\Phi^{BM}$ to either form of fAβ for 30 min showed that $fA\beta_{40}$ yielded an intracellular signal stronger than that of $fA\beta_{42}$ (Fig. 6D vs. E). Increased OPN expression (2.7-fold) along with augmented $fA\beta_{40}$ and $fA\beta_{42}$ uptake by $M\Phi^{BM}$ (2.3- and 2.9-fold, respectively) were detected by qICC analysis (Fig. 6F-H; $p < 0.001 - 0.0001$). Quantitative ELISA analysis of cell lysates validated the qICC results, indicating increased intracellular OPN (2.3-fold; Fig. S6B) with $A\beta_{42}$ uptake elevated 2.5-fold in GA-treated vs. untreated $M\Phi^{BM}$ (Fig. S6C; $p < 0.001$).

To study Aβ phagocytosis in OPN-deficient MΦ, we first knocked down OPN expression using RNA interference (siRNA) (Fig. 6I–K). Previous studies have suggested that intracellular OPN deletion in macrophages impairs general phagocytic activity (Schack et al., 2009; Shin et al., 2011; Toyonaga et al., 2015). Here, to assess OPN involvement in the specific phagocytosis of fAβ, $M\Phi^{BM}$ were first transfected with either $siRNA^{OPN}$ or control $siRNA^{Neg}$, and 48 h later they were exposed to Aβ fibrils. Fluorescent micrographs revealed a substantial reduction of OPN that was associated with decreased $fA\beta_{42}$ uptake by $CD68^+M\Phi^{BM}$ due to siRNA-OPN deficiency (Fig. 6I). The qICC analyses validated our observations and indicated OPN inhibition of 6.8 fold associated with a 2.7 fold reduction in intracellular uptake of $fA\beta_{42}$ (Fig. 6J, K; $p < 0.0001$). Negative control scrambled siRNA did not affect OPN expression or Aβ phagocytosis. The substantial OPN inhibition by siRNA was also confirmed by analysis of protein levels in $M\Phi^{BM}$ cell lysates using quantitative ELISA (Fig. S6D). Importantly, GA treatment failed to increase OPN expression and did not impact $M\Phi^{BM}$ phagocytosis of Aβ fibrils when OPN was knocked down (Fig. 6J, K). Furthermore, taking advantage of a genetic knockout OPN mouse model (KO^{OPN}) allowed us to study $fA\beta_{40}$ and $fA\beta_{42}$ uptake in OPN-deficient $M\Phi^{BM}$ (Fig. 6L, M). Our qICC data suggest that, regardless of GA treatment, phagocytosis of Aβ fibrils is impaired

Fig. 5. Patterns of expression, secretion, and GA-mediated upregulation of OPN in BM-derived macrophage cultures. (A) Schematic illustration of in vitro studies: BM was isolated from WT mice (8- to 12-weeks-old) and cultured for 6 or 7 days in MCSF-enriched media to differentiate into macrophages ($M\Phi^{BM}$). On day 6, cells underwent overnight treatment with GA, siRNA or minocycline, except for untreated control cells (labeled 'C'). On day 7, fibrillar Aβ ($fA\beta_{40}$ or $fA\beta_{42}$) was added in a subset of experiments, followed by phagocytosis assays. Brefeldin A (BFA) treatment was performed 3 h prior to phagocytosis. (B) Constitutive secretion of OPN by $M\Phi^{BM}$ during a 24 h period. Primary $M\Phi^{BM}$ media were collected after 15 min, and then after 1, 4, 6, and 24 h. OPN protein levels were measured at each time point (ELISA; n = 3 wells/time point, 1×10^6 cells/well, in triplicates). (C–E) Intracellular OPN expression in $M\Phi^{BM}$. Scale bars = 10μm. Representative fluorescent micrographs of $M\Phi^{BM}$ immunostained for OPN, (C) early endosomal antigen (EEA1) marker, (D) late endosome-lysosomal marker Ras-related protein (Rab7), or (E) Golgi marker 58 K protein, and nuclei (DAPI). The merged images demonstrate subcellular OPN expression within vesicles, predominantly confined to the trans-Golgi network (yellow punctate signal). (F–J) Upregulation of OPN in $M\Phi^{BM}$ by GA treatment. (F, G) Representative fluorescent micrographs demonstrate the effect of GA treatment on $M\Phi^{BM}$ expression of OPN in the absence of Aβ, either (F) without BFA treatment or (G) with BFA pre-treatment. $M\Phi^{BM}$ were immunostained for OPN (red), which was more highly expressed following GA treatment. (F: insert) Subcellular OPN within transport vesicles in $M\Phi^{BM}$. (G) Round-shaped $M\Phi^{BM}$ after BFA inhibition of OPN secretion. Scale bars: 20 μm, insert scale 5 μm. (H) Quantitative ICC of OPN-immunoreactive area revealed a significant upregulation of OPN in $M\Phi^{BM}$ following GA treatment, with or without BFA inhibition. Means of individual cell fluorescent areas are indicated (n = 5–9 images/well, average 100 cells/image, and n = 3–5 wells/treatment group). (I) Western blot image of cell lysates from above-mentioned experimental groups. (J) Corresponding densitometry results of OPN levels in Western blots (normalized to β-actin levels; n = 3 wells/group, 1×10^6 cells/well; repeated experiments). Group means, SEMs and individual data points are shown. Fold increases in mean values compared with controls indicated in red. $^*p < 0.05$, $^{**}p < 0.01$, $^{***}p < 0.001$, $^{****}p < 0.0001$, by one-way ANOVA and Dunnett's multiple comparisons post-tests.

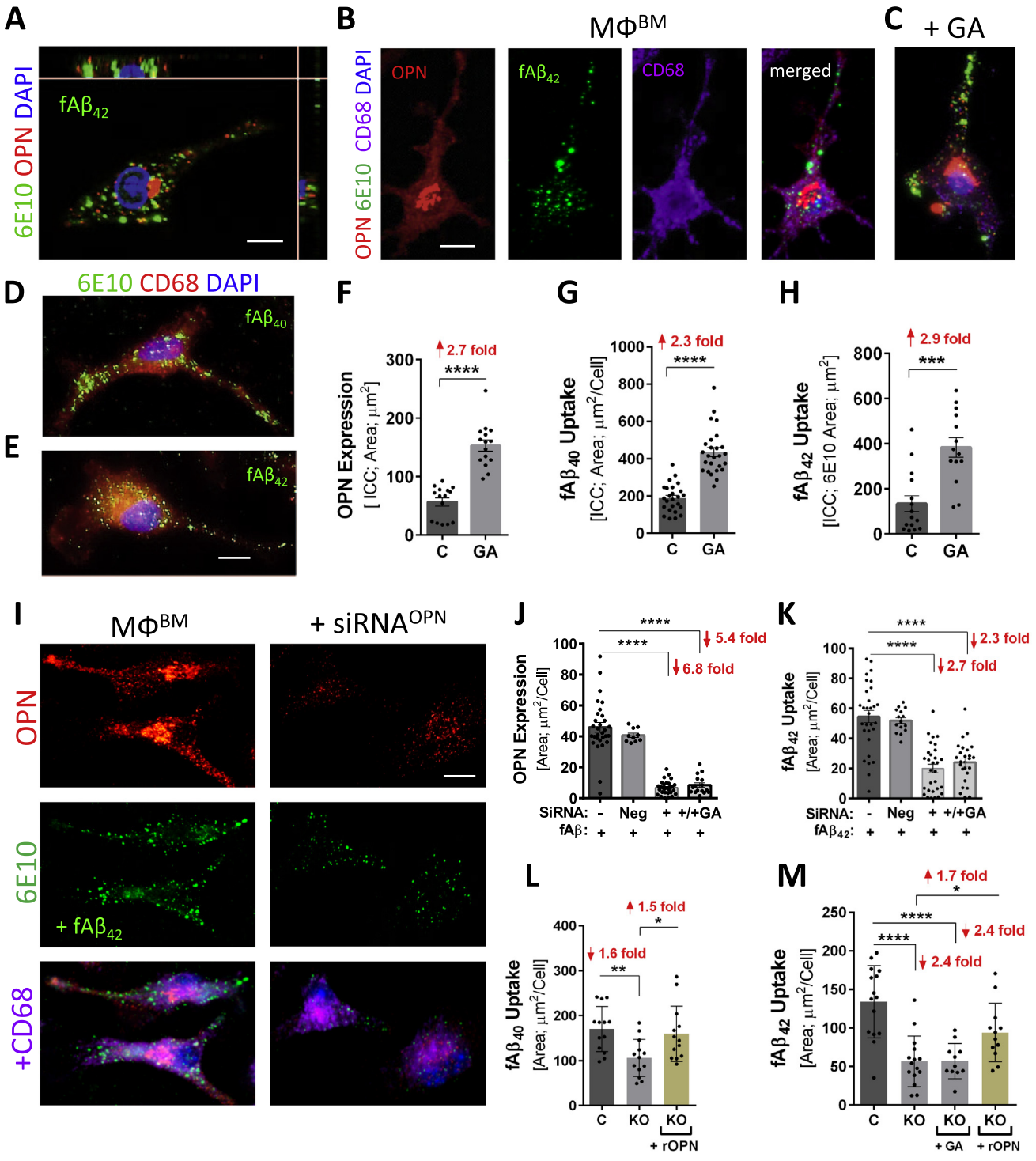

Fig. 6. Phagocytosis of $A\beta_{40}$ and $A\beta_{42}$ fibrils by BM-derived macrophages is dependent on OPN expression. (A–H) Representative fluorescent micrographs and quantitative analyses of OPN expression and Aβ uptake in $CD68^+$ $M\Phi^{BM}$, in primary cultures pre-treated with GA for 24 h and stimulated with fibrillar (f)$A\beta_{40}$ or $fA\beta_{42}$ for 30 min. Scale bars: 10 µm. (A) Higher magnification Z-stack image shows intracellular uptake of $6E10^+$-Aβ along with subcellular OPN expression patterns in untreated $M\Phi^{BM}$. (B, C) Increased OPN expression and enhanced cellular uptake of $fA\beta_{42}$ was detected following GA treatment. (D, E) Representative images display phagocytosis of $fA\beta_{40}$ vs. $fA\beta_{42}$ by untreated $M\Phi^{BM}$. (F–H) Quantitative ICC analysis of average OPN expression (F), intracellular $fA\beta_{40}$ (G), and $fA\beta_{42}$ (H) areas per $M\Phi^{BM}$ in GA-treated vs. untreated $M\Phi^{BM}$. Along with increased OPN expression, $M\Phi^{BM}$ pre-treated with GA exhibit enhanced uptake of Aβ fibrils. (I) Representative micrographs of OPN-silenced $M\Phi^{BM}$ (via $siRNA^{OPN}$ knockdown) vs. untreated cells reveal reduced $fA\beta_{42}$ phagocytosis. Scale bar: 10 µm. (J, K) Quantitative ICC revealed that silenced expression of OPN via $siRNA^{OPN}$ leads to impaired $fA\beta_{42}$ phagocytosis in $M\Phi^{BM}$, regardless of GA treatment. Negative control scrambled $siRNA^{Neg}$ affected neither OPN expression nor fAβ phagocytosis. (L, M) Additional experiment utilizing $M\Phi^{BM}$ isolated from OPN knockout (KO) mice vs. WT mice (controls, C). Quantitative ICC analysis of intracellular $fA\beta_{40}$ and $fA\beta_{42}$ uptake in control $M\Phi^{BM}$, OPN-deficient $M\Phi^{BM}$ (KO), and GA-treated OPN-deficient $M\Phi^{BM}$ (KO + GA). OPN-deficient $M\Phi^{BM}$ exhibit impaired fAβ phagocytosis, partially restored by supplementation of human recombinant (r) OPN. Means of individual cell fluorescent areas indicated (average of n = 5–10 images per well, with ~100 cells/image, n = 4–6 wells/treatment group). Group means, SEMs and individual data points are shown. Fold increases in mean values compared with controls indicated in red. $^{*}p < 0.05$, $^{**}p < 0.01$, $^{***}p < 0.001$, $^{****}p < 0.0001$, by one-way ANOVA and Tukey's multiple comparisons post-tests or two-tail unpaired Student's *t*-test.

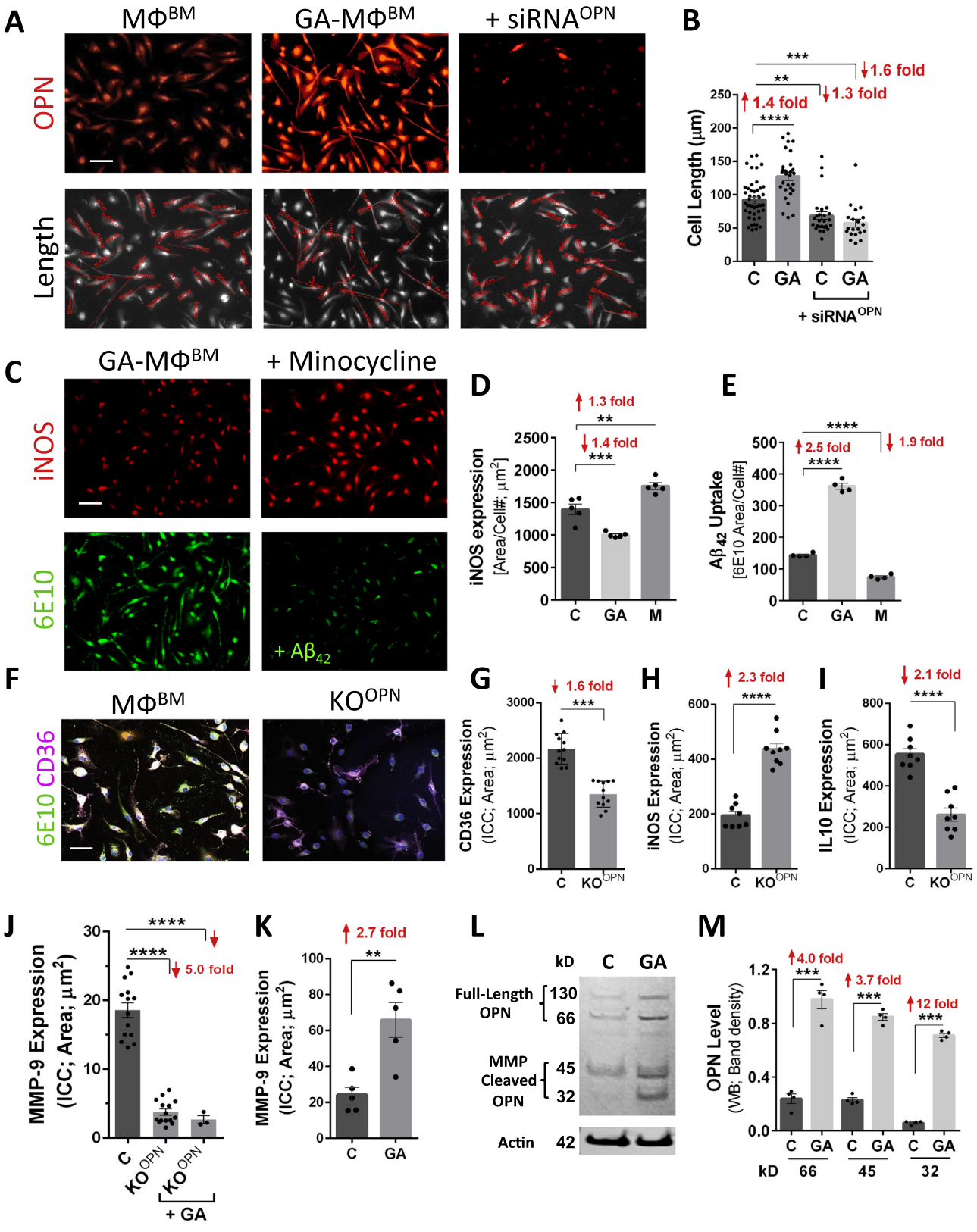
A
MΦBM
GA-MΦBM
+ siRNAOPN
OPN
Length
B
Cell Length (μm)
1.4 fold
1.3 fold
1.6 fold
C GA C GA
+ siRNAOPN
C
GA-MΦBM
+ Minocycline
iNOS
6E10
+ Aβ42
D
iNOS expression [Area/Cell#; μm2]
1.3 fold
1.4 fold
C GA M
E
Aβ42 Uptake [6E10 Area/Cell#]
2.5 fold
1.9 fold
C GA M
F
MΦBM
KOOPN
6E10 CD36
G
CD36 Expression (ICC; Area; μm2)
1.6 fold
C KOOPN
H
iNOS Expression (ICC; Area; μm2)
2.3 fold
C KOOPN
I
IL10 Expression (ICC; Area; μm2)
2.1 fold
C KOOPN
J
MMP-9 Expression (ICC; Area; μm2)
5.0 fold
C KOOPN KOOPN + GA
K
MMP-9 Expression (ICC; Area; μm2)
2.7 fold
C GA
L
kD C GA
Full-Length OPN 130 66
MMP Cleaved OPN 45 32
Actin 42
M
OPN Level (WB; Band density)
4.0 fold
3.7 fold
12 fold
C GA C GA C GA
kD 66 45 32

in the absence of OPN (Fig. 6L, M). Notably, addition of full-length rOPN (50 ng/mL, overnight) to KO^{OPN}-$M\Phi^{BM}$ reversed their impairment in cellular uptake of $fA\beta_{40}$ and $fA\beta_{42}$ (Fig. 6L, M; $p < 0.05$). Overall, these results reveal that phagocytosis of pathogenic Aβ alloforms by $M\Phi^{BM}$ is OPN-dependent, and that upon exposure to GA, it undergoes a gain-of-function mediated by elevated OPN expression.

3.6. OPN plays a key role in macrophage polarization towards an anti-inflammatory phenotype

Macrophages, as well as their circulating counterparts, monocytes, make up a highly heterogeneous population that can acquire various phenotypes and biological functions in response to environmental signals [reviewed in Gliem et al. (2016)]. To further elucidate OPN's effects on $M\Phi^{BM}$-mediated Aβ phagocytosis, we investigated whether these effects relate to larger morphological and immunological profile alterations. Past studies have reported that OPN induces $M\Phi^{BM}$ to differentiate into the anti-inflammatory M2 phenotype (Tambuyzer et al., 2012), a polarization associated with elongated cell morphology (McWhorter et al., 2013). Analysis of $M\Phi^{BM}$ cell length under various treatment conditions, including OPN-induction by GA and -silencing by siRNA, revealed significant changes in $CD68^{+}M\Phi^{BM}$ cell length as displayed in the representative fluorescent micrographs (Fig. 7A). While GA induced OPN expression, it also increased $M\Phi^{BM}$ cell elongation by 1.4 times (Fig. 7B; $p < 0.0001$). In contrast, $siRNA^{OPN}$ knockdown reversed GA's effects and further decreased cell length by 1.3 times (Fig. 7B; $p < 0.01$). In the absence of OPN, GA did not affect $M\Phi^{BM}$ cell elongation (Fig. 7B; $p < 0.001$), in agreement with our previous Aβ phagocytosis results (Fig. 6K).

We next assessed the expression of inducible nitric oxide synthase (iNOS), a hallmark of pro-inflammatory M1 macrophages, in different treatment groups; we used the tricyclic antibiotic minocycline to suppress OPN expression (Fig. 7C–E). Minocycline has been shown to modulate inflammatory response, and to reduce MMP-9 activity and generation of proteolytic OPN fragments (Chan et al., 2014). $M\Phi^{BM}$ underwent either OPN-activation by GA or -inhibition by minocycline, and were then exposed to fibrillar $A\beta_{42}$ for 30 min. Fluorescent micrographs demonstrate that GA reduced iNOS expression and increased fibrillar $A\beta_{42}$ phagocytosis, while minocycline induced opposite effects (Fig. 7C). Quantitative ICC assays confirmed a significant 1.3-fold increase in iNOS expression by minocycline-treated macrophages, and a substantial 1.9-fold reduction in $A\beta_{42}$ phagocytosis (Fig. 7D, E; $p < 0.01 - 0.0001$). GA treatment reduced iNOS 1.4-fold but boosted Aβ phagocytosis 2.5-fold (Fig. 7D, E; $p < 0.001 - 0.0001$).

Furthermore, we analyzed $M\Phi^{BM}$ phenotype in the genetic OPN-null (KO^{OPN}) models. Downregulation of OPN in the KO^{OPN}-$M\Phi^{BM}$ was accompanied by impaired ability to uptake $fA\beta_{42}$ (Figs. 6L, M and 7F). KO^{OPN}-$M\Phi^{BM}$ showed a significant 1.6-fold reduction in surface expression of the scavenger receptor CD36 (implicated in Aβ phagocytosis), a 2.3-fold increase in proinflammatory iNOS expression, and 2.1-fold decrease in anti-inflammatory cytokine interleukine-10 expression (Fig. 7G–I; $p < 0.001 - 0.0001$) in comparison with control-$M\Phi^{BM}$. These studies demonstrate that OPN silencing, either by siRNA, minocycline, or genetic knock-out (KO^{OPN}), all of which impaired macrophages' ability to uptake Aβ fibrils, was associated with a proinflammatory profile. Importantly, induction of OPN expression by GA induced polarization towards the anti-inflammatory, highly phagocytic macrophage phenotype with elongated pro-healing cell morphology.

In addition to phagocytosis, enzymatic degradation is another major mechanism through which $M\Phi^{BM}$ can clear Aβ. It has been shown that MMP-9 degrades Aβ, associates with an alternatively-activated macrophage phenotype, and is regulated by and directly cleaves OPN to generate biologically-active products (Agnihotri et al., 2001; Tan et al., 2013). Quantitative ICC analysis in OPN-deficient (KO^{OPN})-$M\Phi^{BM}$ showed a substantial 5-fold decrease in MMP-9 expression (Fig. 7J; $p < 0.0001$); under OPN loss-of-function conditions, GA treatment failed to reverse MMP-9 levels. In agreement with our previous results (Koronyo et al., 2015), GA treatment significantly increased MMP-9 expression 2.7-fold in WT-$M\Phi^{BM}$ (Fig. 7K; $p < 0.01$); representative Z-stack images show a remarkable increase in MMP-9 expression in GA-treated $M\Phi^{BM}$ (Fig. S6E). Abundant MMP-9 expression, increased fAβ phagocytosis, and a 3.1-fold elevation of surface scavenger receptor SCARA-1 are shown in GA-treated $M\Phi^{BM}$ (Fig. S6F, G; $p < 0.0001$). These results mirror our in vivo correlation analysis of ADtg mouse brains, showing a strong linear relationship between OPN and MMP-9 (Fig. S4E, F), which was even tighter between cortex-infiltrating OPN-expressing $CD45^{hi}$ cells and local MMP-9 levels (Fig. S4G).

Moreover, we analyzed OPN protein levels in $M\Phi^{BM}$ using a polyclonal antibody recognizing the full-length OPN and its MMP-cleaved fragments, including the anti-inflammatory 32 kD C-terminus fragment (Chan et al., 2014; Scatena et al., 2007). Western blot analysis and subsequent quantification of band densities revealed that all OPN forms, including fragments derived from MMPs' proteolysis, were elevated by GA treatment (Fig. 7L, M). Interestingly, the MMP-generated 32kD C-terminus-containing

Fig. 7. OPN promotes an anti-inflammatory, pro-healing phenotype in BM-derived macrophages. (A) Fluorescent micrographs of $M\Phi^{BM}$ in primary cultures, either untreated, pretreated overnight with GA, or silenced with $siRNA^{OPN}$, were immunostained for OPN (upper panel). Lower panel displays grayscale images of $CD68^{+}M\Phi^{BM}$ with cell length measurements (red) by Zeiss Axiovision software. (B) Quantitative analysis of cell length measurements. Mean and individual cell lengths shown (n = 20–46 counts, n = 3–4 wells/group). Elongated cell processes in $M\Phi^{BM}$ are linked with polarization towards a highly phagocytic, pro-healing phenotype, resulting from amplified OPN expression following GA treatment. OPN inhibition by siRNA produced shorter cells, and under the resulting OPN deficiency, not even GA treatment could restore their elongated morphology. (C) Fluorescent images of $M\Phi^{BM}$ treated with GA or minocycline (M) for 24 h and then exposed to $fA\beta_{42}$ for 30 min. Cells immunostained for inducible nitric oxide synthase (iNOS) and Aβ (6E10). (D, E) Quantitative ICC revealed that minocycline treatment increased iNOS expression, which in turn reduced $fA\beta_{42}$ phagocytosis. (F–J) Altered phenotype of OPN-knockout $M\Phi^{BM}$ (KO^{OPN}). (F) Representative fluorescent micrographs of control vs. KO^{OPN}-$M\Phi^{BM}$ labeled for Aβ (6E10), scavenger receptor CD36, and nuclei (DAPI). Reduced $fA\beta_{42}$ uptake in KO^{OPN}-$M\Phi^{BM}$ is associated with significant decrease in surface CD36 expression (G). Quantitative ICC analysis of (H) iNOS, (I) interleukin 10 (IL10), and (J) matrix metalloproteinase 9 (MMP9) in control vs. KO^{OPN}-$M\Phi^{BM}$. Reduced OPN expression in KO-$M\Phi^{BM}$ altered their immunological profile; addition of GA did not affect MMP9 expression in KO^{OPN}-$M\Phi^{BM}$. (K) Quantitative ICC reveals increase in MMP-9 following GA treatment in WT $M\Phi^{BM}$. Means of individual cell fluorescent areas are indicated (n = 5–10 images/well, average 100 cells/image, n = 3–5 wells/group). (L) OPN levels as determined by Western blot with rabbit anti-OPN antibody. (M) Respective quantitative band density analysis shows elevation of OPN fragments derived from metalloproteinase (MMP) proteolysis following GA treatment, consistent with elevated MMP-9 production (normalized to β-actin input; n = 4 wells/group, 1×10^6 cells/well; repeated experiments). Secretion and proteolysis of OPN by $M\Phi^{BM}$ polarized towards an anti-inflammatory phenotype (mediated by MMP) amplified $fA\beta_{42}$ phagocytosis. Group means, SEMs and individual data points are shown. Fold increases in mean values compared with controls indicated in red. Scale bars: 50 μm. $^{**}p < 0.01$, $^{***}p < 0.001$, $^{****}p < 0.0001$, by one-way ANOVA and Tukey's multiple comparisons post tests or two-tail unpaired Student's *t*-test.

OPN form was elevated 12-fold after GA treatment (Fig. 7M; $p < 0.001$). This fragment's basal levels were very low in untreated $M\Phi^{BM}$, but rose in prominence after GA activation (Fig. 7M). The combined data suggest that OPN affects various aspects of macrophages' immunological profile, including polarization towards a pro-healing, anti-inflammatory, highly phagocytic phenotype.

4. Discussion

In this study, we identified OPN's novel role as a major contributor to Aβ clearance through elevated monocyte-macrophage recruitment into ADtg mouse brains and promotion of macrophage polarization towards an anti-inflammatory, highly phagocytic phenotype. Using both in vivo and in vitro AD models, we demonstrated that treatment with the FDA-approved drug GA effectively upregulates OPN expression in macrophages and boosts phagocytosis of Aβ. OPN showed an expression pattern specific to brain regions associated with AD (hippocampus and cortex), was predominantly detected in infiltrating monocytes and macrophages, and increased during aging – especially in diseased ADtg mice. Moreover, in brain tissues from AD patients, we also identified increased OPN within myelomonocytic cells surrounding Aβ lesion sites, mirroring our results in ADtg mice. Our flow cytometry analysis of blood and brain myelomonocytic cells in ADtg mice showed a GA-induced enrichment of OPN^+ monocyte subpopulations in the blood ($CD115^+CD11b^+Ly6C^{high}$) and, most importantly, in the brain ($CD11b^+Ly6C^+CD45^{high}$). Indeed, histological analysis confirmed that OPN was primarily expressed in brain-infiltrating $Iba1^+CD45^{high}$ or GFP-labeled monocytes and macrophages, but also to a lesser extent in $Iba1^+CD45^{low\text{-}mid}$ microglia. Our in vitro studies substantiated the in vivo findings by demonstrating that macrophage-mediated Aβ clearance is OPN-dependent: upon gain-of-function, it promotes a phenotype that is highly phagocytic of Aβ and anti-inflammatory, while its inhibition impairs uptake of Aβ fibrils and hinders the neuroprotective effects of GA on macrophage immunological profile. Our multiple correlation analyses strongly suggest that OPN is an immunomodulatory cytokine relevant to resisting AD pathology. It shows tight links to increases in brain-infiltrating monocytes and levels of monocyte-chemoattractant MCP-1, to decreases in soluble/insoluble vascular and parenchymal Aβ burden, and to a macrophage phenotype notable for overexpression of MMP-9. This study urges further investigation of OPN as a tool for therapeutic intervention targeting myelomonocytic cells in AD.

Although increased OPN expression has been detected in reactive microglia following traumatic brain injury (Chan et al., 2014) and in ADtg mouse brains (Keren-Shaul et al., 2017; Yin et al., 2017), here we observed that cerebral OPN expression in AD patients and murine models increases predominantly in monocytes and macrophages compared to the activated microglia surrounding Aβ plaques. This observation is consistent with studies demonstrating that blood-borne infiltrating macrophages phagocytose Aβ plaques more efficiently than do resident microglia (Bernstein et al., 2014; Butovsky et al., 2007; Koronyo et al., 2015; Koronyo-Hamaoui et al., 2009; Majumdar et al., 2008). Two recent reports were unable to demonstrate the impact of brain-infiltrating monocyte/macrophages on reducing cerebral Aβ burden; however, these studies involved invasive techniques and/or compounds that depleted brain microglia (Prokop et al., 2015; Varvel et al., 2015), possibly eliminating the local signals to attract monocytes to Aβ lesion sites (Shechter et al., 2009). In contrast, growing evidence from genetic, physiologic, and histological studies overwhelmingly support the key role of peripheral monocytes in cerebral Aβ clearance (Bernstein et al., 2014; Butovsky et al., 2007; El Khoury et al., 2007; Koronyo et al., 2015; Koronyo-Hamaoui et al., 2009; Lai and McLaurin, 2012; Lebson et al., 2010; Malm et al., 2012; Simard et al., 2006). OPN's known interactions with various surface integrins and scavenger receptors [reviewed in (Rittling, 2011)] further support its direct effects on the phagocytic activity of these inflammatory cells. Notably, the marked upregulation of cerebral OPN following GA immunization was even greater when combined with intravenous $CD115^+$ monocyte enrichment. These results parallel our previous report of increased monocyte recruitment to the brain (defined by CD115, Ly6C, and CD45 biomarkers) brought on synergistically through the combination of these immunomodulatory approaches (Koronyo et al., 2015). Given that OPN is an integrin-binding protein expressed by macrophages, our findings could explain its action in opsonization and recruitment of immune cells to inflammatory sites (Kahles et al., 2014; Lund et al., 2009; Rittling, 2011). Therefore, we conclude that when GA induces recruitment of peripheral phagocytic cells to amyloid plaques, this immunomodulatory phenomenon is mediated by OPN.

This study indicates that GA substantially induces OPN expression in BM-derived macrophages in a manner similar to that observed in brains of ADtg mice. We also found consistent evidence for increased OPN and subsequent intracellular uptake of pre-formed $A\beta_{40}$ and $A\beta_{42}$ fibrils by these GA-stimulated primary cultures. As expected, the cytokine OPN was mostly localized to macrophages within the major secretory pathway, the trans-Golgi network vesicles (Verhulst et al., 2002), indicating that it is constantly expressed and, perhaps, sorted for post-translation modifications prior to secretion. This pattern of intracellular OPN expression was different from that of the endosomal-lysosomal localization of $A\beta_{40}$ and $A\beta_{42}$ fibrils following phagocytosis. By utilizing systems that negatively regulate OPN expression (siRNA, genetic $OPN^{-/-}$, or minocycline) or positively induce it with GA or supplementation of rOPN (Suzuki et al., 2010), we have demonstrated OPN's crucial role in macrophage-mediated Aβ phagocytosis. These results, along with literature describing OPN's involvement in other phagocytic activities, reveal that fibrillar Aβ phagocytosis may directly depend on OPN expression (Shin et al., 2011; Toyonaga et al., 2015).

Different functions of OPN may be achieved through its complex proteolytic processing, such as cleavage by MMPs that permits diverse cellular interactions. Specifically, MMP-9 has been implicated in generating functional, more neuroprotective fragments of OPN then the full length OPN (Chan et al., 2014; Scatena et al., 2007). Our data indicate that the dramatic reduction of MMP-9 expression following OPN inhibition cannot be recovered by GA, implying that GA's mechanistic effects are mediated by OPN. In WT macrophages, GA not only induced MMP-9 expression, but also significantly increased the abundance of full-length OPN and its MMP-cleaved fragments. In agreement with previous studies (Ge et al., 2017; Sun et al., 2013), our results support the notion that OPN and MMP-9 have an intricate relationship, regulating each other's expression levels or functions. Our examination of infiltrating Mo/MΦ in ADtg mouse brains further supports the connection between MMP-9 and OPN, evidenced by their tight correlation and increased expression following GA immunization. These findings align with reports from various groups, all of which indicate MMP-9′s role in generating functional forms of OPN (Chan et al., 2014; Scatena et al., 2007; Tambuyzer et al., 2012). It is possible that macrophages may control neuroinflammation through release of MMP-9, which in turn cleaves full-length OPN to generate potent immunoregulatory C-terminal OPN fragments. While future studies should ascertain how each OPN fragment may impact macrophage phenotype in the context of AD, we postulate that GA's induction of a therapeutic macrophage phenotype is mediated by elevating these MMP-cleaved neuroprotective fragments of OPN.

Although generally regarded as a pro-inflammatory cytokine, recent studies have shown that OPN may contribute to repair-promoting processes in the brain (Albertsson et al., 2014; Chan et al., 2014; Meller et al., 2005; Shin et al., 2011; van Velthoven et al., 2011). This study unexpectedly demonstrated that GA polarizes macrophages towards a phenotype that is highly phagocytic (increased uptake of fibrillar Aβ and associated surface scavenger receptors), anti-inflammatory (reduced iNOS and increased IL-10 and MMP-9), and pro-healing (elongated), a process dependent on OPN expression. Upon inhibition of OPN, this phenotype shift was reversed. Since OPN is known to suppress production of NO and iNOS [reviewed in Rittling (2011)], it was no surprise that OPN inhibition resulted in increased iNOS while OPN elevation (via GA) decreased iNOS. Beyond anti-inflammatory IL-10 induction, elevated OPN expression and consequent down-regulation of NO/iNOS may present a mechanism by which macrophages minimize neuroinflammation in AD. Our previous reports of the marked therapeutic effects of GA on cognitive function in ADtg mice (Bakalash et al., 2011; Butovsky et al., 2006, 2007; Koronyo et al., 2015; Zuroff et al., 2017) warrant future studies to elucidate OPN's potential impact on synaptic and cognitive preservation in vivo. Collectively, we have demonstrated a novel role for OPN as a key immune-regulator of macrophage phenotype and Aβ clearance in AD models. The specific OPN-dependence of macrophage polarization suggests that this cytokine is a potential key neuroprotectant involved in resisting AD-related pathology and promoting tissue repair.

Compliance with ethical standards

Financial support

This work was funded by the Coins for Alzheimer's Research Trust (C.A.R.T.) Fund, The BrightFocus Foundation, The Maurice Marciano Family Foundation, The Saban Family Foundation, and the National Center for Advancing Translational Sciences CTSI Grant.

Ethical approval

All applicable international, national, and/or institutional guidelines for the care and use of animals were followed. All procedures performed in studies involving animals were in accordance with the ethical standards of the institution at which the studies were conducted. This article does not contain any studies with human participants performed by any of the authors.

Author contributions

M.K.-H.: Study conception, design and supervision. A.R., M.K.-H.: Major experimental contribution, planning, data acquisition and analysis. Y.K., J.S, D.-T.F, B.C.S.: Other important experimental contribution, image acquisition, flow cytometry, and/or data analysis; S.L.: assistance with siRNA experiments; E.Y.H., D.B.T: help with fibrillar Aβ preparations and rOPN experiments; M.K.-H., A.R, Y.K. J.S, D.-T.F, H.E.S. N.J.H., D.D: Data analysis, interpretation, and presentation; M.K.-H.: Discussion on intellectual content, supervision, and manuscript editing. M.K.H., Y.K., J.S., D.-T.F, N.J.H. and A.R.: Manuscript editing, figure preparation, and revision. M.K.-H., A.R.: Figure preparation, manuscript writing, revision, and final approval.

Dedication

This paper is dedicated to the memory of Dr. Salomon Moni Hamaoui and Lillian Jones Black, both of whom died from Alzheimer's disease.

Conflict of interest

Authors declare no conflict of interest. International patent application PCT/US2017/033875 filed in the United States 5/22/2017. Legal Ref: 065472.000611WO00. *Inventors:* Koronyo M, Rentsendorj A, Black KL, and Koronyo, Y.

Acknowledgments

We would like to thank Dror Berel for assistance in multi-factor correlation analyses, Dr. Carol Miller for providing human brain tissue samples, Dr. Andrea Wolf for providing cells for a subset of bone marrow macrophage experiments, Dr. Hassanzadeh-Kiabi Nargess for assistance in flow cytometry analysis, and Ms. Mia Oviatt for editing assistance.

Appendix A. Supplementary data

Supplementary data associated with this article can be found, in the online version, at http://dx.doi.org/10.1016/j.bbi.2017.08.019.

References

Agnihotri, R., Crawford, H.C., Haro, H., Matrisian, L.M., Havrda, M.C., Liaw, L., 2001. Osteopontin, a novel substrate for matrix metalloproteinase-3 (stromelysin-1) and matrix metalloproteinase-7 (matrilysin). J. Biol. Chem. 276, 28261–28267.

Albertsson, A.M., Zhang, X., Leavenworth, J., Bi, D., Nair, S., Qiao, L., Hagberg, H., Mallard, C., Cantor, H., Wang, X., 2014. The effect of osteopontin and osteopontin-derived peptides on preterm brain injury. J. Neuroinflammation 11, 197.

Bakalash, S., Pham, M., Koronyo, Y., Salumbides, B.C., Kramerov, A., Seidenberg, H., Berel, D., Black, K.L., Koronyo-Hamaoui, M., 2011. Egr1 expression is induced following glatiramer acetate immunotherapy in rodent models of glaucoma and Alzheimer's disease. Invest. Ophthalmol. Visual Sci. 52, 9033–9046.

Bateman, R.J., Xiong, C., Benzinger, T.L., Fagan, A.M., Goate, A., Fox, N.C., Marcus, D.S., Cairns, N.J., Xie, X., Blazey, T.M., Holtzman, D.M., Santacruz, A., Buckles, V., Oliver, A., Moulder, K., Aisen, P.S., Ghetti, B., Klunk, W.E., McDade, E., Martins, R. N., Masters, C.L., Mayeux, R., Ringman, J.M., Rossor, M.N., Schofield, P.R., Sperling, R.A., Salloway, S., Morris, J.C., 2012. Clinical and biomarker changes in dominantly inherited Alzheimer's disease. N. Engl. J. Med. 367, 795–804.

Bernstein, K.E., Koronyo, Y., Salumbides, B.C., Sheyn, J., Pelissier, L., Lopes, D.H., Shah, K.H., Bernstein, E.A., Fuchs, D.T., Yu, J.J., Pham, M., Black, K.L., Shen, X.Z., Fuchs, S., Koronyo-Hamaoui, M., 2014. Angiotensin-converting enzyme overexpression in myelomonocytes prevents Alzheimer's-like cognitive decline. J. Clin. Invest. 124, 1000–1012.

Bilgel, M., An, Y., Zhou, Y., Wong, D.F., Prince, J.L., Ferrucci, L., Resnick, S.M., 2016. Individual estimates of age at detectable amyloid onset for risk factor assessment. Alzheimers Dement. J. Alzheimers Assoc. 12, 373–379.

Brown, A., 2012. Osteopontin: a key link between immunity, inflammation and the central nervous system. Transl. Neurosci. 3, 288–293.

Butovsky, O., Koronyo-Hamaoui, M., Kunis, G., Ophir, E., Landa, G., Cohen, H., Schwartz, M., 2006. Glatiramer acetate fights against Alzheimer's disease by inducing dendritic-like microglia expressing insulin-like growth factor 1. Proc. Natl. Acad. Sci. U.S.A. 103, 11784–11789.

Butovsky, O., Kunis, G., Koronyo-Hamaoui, M., Schwartz, M., 2007. Selective ablation of bone marrow-derived dendritic cells increases amyloid plaques in a mouse Alzheimer's disease model. Eur. J. Neurosci. 26, 413–416.

Chan, J.L., Reeves, T.M., Phillips, L.L., 2014. Osteopontin expression in acute immune response mediates hippocampal synaptogenesis and adaptive outcome following cortical brain injury. Exp. Neurol. 261, 757–771.

Choi, J.S., Kim, H.Y., Cha, J.H., Choi, J.Y., Lee, M.Y., 2007. Transient microglial and prolonged astroglial upregulation of osteopontin following transient forebrain ischemia in rats. Brain Res. 1151, 195–202.

Comi, C., Carecchio, M., Chiocchetti, A., Nicola, S., Galimberti, D., Fenoglio, C., Cappellano, G., Monaco, F., Scarpini, E., Dianzani, U., 2010. Osteopontin is increased in the cerebrospinal fluid of patients with Alzheimer's disease and its levels correlate with cognitive decline. J. Alzheimers Dis. JAD 19, 1143–1148.

De Strooper, B., Karran, E., 2016. The cellular phase of Alzheimer's disease. Cell 164, 603–615.

El Khoury, J., Toft, M., Hickman, S.E., Means, T.K., Terada, K., Geula, C., Luster, A.D., 2007. Ccr2 deficiency impairs microglial accumulation and accelerates progression of Alzheimer-like disease. Nat. Med. 13, 432–438.

Ellis, R.J., Olichney, J.M., Thal, L.J., Mirra, S.S., Morris, J.C., Beekly, D., Heyman, A., 1996. Cerebral amyloid angiopathy in the brains of patients with Alzheimer's disease: the CERAD experience, part XV. Neurology 46, 1592–1596.

Franzen, A., Heinegard, D., 1985. Isolation and characterization of two sialoproteins present only in bone calcified matrix. Biochem. J. 232, 715–724.

Frenkel, D., Maron, R., Burt, D.S., Weiner, H.L., 2005. Nasal vaccination with a proteosome-based adjuvant and glatiramer acetate clears beta-amyloid in a mouse model of Alzheimer disease. J. Clin. Invest. 115, 2423–2433.
Ge, Q., Ruan, C.C., Ma, Y., Tang, X.F., Wu, Q.H., Wang, J.G., Zhu, D.L., Gao, P.J., 2017. Osteopontin regulates macrophage activation and osteoclast formation in hypertensive patients with vascular calcification. Sci. Rep. 7, 40253.
Glenner, G.G., Wong, C.W., Quaranta, V., Eanes, E.D., 1984. The amyloid deposits in Alzheimer's disease: their nature and pathogenesis. Appl. Pathol 2, 357–369.
Gliem, M., Krammes, K., Liaw, L., van Rooijen, N., Hartung, H.P., Jander, S., 2015. Macrophage-derived osteopontin induces reactive astrocyte polarization and promotes re-establishment of the blood brain barrier after ischemic stroke. Glia 63, 2198–2207.
Gliem, M., Schwaninger, M., Jander, S., 2016. Protective features of peripheral monocytes/macrophages in stroke. Biochim. Biophys. Acta 1862, 329–338.
Hardy, J., Duff, K., Hardy, K.G., Perez-Tur, J., Hutton, M., 1998. Genetic dissection of Alzheimer's disease and related dementias: amyloid and its relationship to tau. Nat. Neurosci. 1, 355–358.
Hart, N.J., Koronyo, Y., Black, K.L., Koronyo-Hamaoui, M., 2016. Ocular indicators of Alzheimer's: exploring disease in the retina. Acta Neuropathol. 132, 767–787.
Herzig, M.C., Van Nostrand, W.E., Jucker, M., 2006. Mechanism of cerebral beta-amyloid angiopathy: murine and cellular models. Brain Pathol. 16, 40–54.
Kahles, F., Findeisen, H.M., Bruemmer, D., 2014. Osteopontin: a novel regulator at the cross roads of inflammation, obesity and diabetes. Mol. Metab. 3, 384–393.
Keren-Shaul, H., Spinrad, A., Weiner, A., Matcovitch-Natan, O., Dvir-Szternfeld, R., Ulland, T.K., David, E., Baruch, K., Lara-Astaiso, D., Toth, B., Itzkovitz, S., Colonna, M., Schwartz, M., Amit, I., 2017. A unique microglia type associated with restricting development of alzheimer's disease. Cell 169, 1276–1290.
Kim, M.D., Cho, H.J., Shin, T., 2004. Expression of osteopontin and its ligand, CD44, in the spinal cords of Lewis rats with experimental autoimmune encephalomyelitis. J. Neuroimmunol. 151, 78–84.
Koronyo, Y., Salumbides, B.C., Sheyn, J., Pelissier, L., Li, S., Ljubimov, V., Moyseyev, M., Daley, D., Fuchs, D.T., Pham, M., Black, K.L., Rentsendorj, A., Koronyo-Hamaoui, M., 2015. Therapeutic effects of glatiramer acetate and grafted CD115 (+) monocytes in a mouse model of Alzheimer's disease. Brain J. Neurol. 138, 2399–2422.
Koronyo, Y., B, D., Barron, E., Boyer, D.S., Pearlman, J.A., Au, W.J., Kile, S.J., Blanco, A., Fuchs, D.T., Ashfaq, A., Frautschy, S., Cole, G.M., Miller, C.A., Hinton, D.R., Verdooner, S.R., Black, K.L., Koronyo-Hamaoui, M., 2017. Retinal amyloid pathology and proof-of-concept imaging trial in Alzheimer's disease. JCI Insight 2, e93621.
Koronyo-Hamaoui, M., Ko, M.K., Koronyo, Y., Azoulay, D., Seksenyan, A., Kunis, G., Pham, M., Bakhsheshian, J., Rogeri, P., Black, K.L., Farkas, D.L., Schwartz, M., 2009. Attenuation of AD-like neuropathology by harnessing peripheral immune cells: local elevation of IL-10 and MMP-9. J. Neurochem. 111, 1409–1424.
Koronyo-Hamaoui, M., Koronyo, Y., Ljubimov, A.V., Miller, C.A., Ko, M.K., Black, K.L., Schwartz, M., Farkas, D.L., 2011. Identification of amyloid plaques in retinas from Alzheimer's patients and noninvasive in vivo optical imaging of retinal plaques in a mouse model. Neuroimage 54 (Suppl 1), S204–217.
La Morgia, C., Ross-Cisneros, F.N., Koronyo, Y., Hannibal, J., Gallassi, R., Cantalupo, G., Sambati, L., Pan, B.X., Tozer, K.R., Barboni, P., Provini, F., Avanzini, P., Carbonelli, M., Pelosi, A., Chui, H., Liguori, R., Baruzzi, A., Koronyo-Hamaoui, M., Sadun, A.A., Carelli, V., 2016. Melanopsin retinal ganglion cell loss in Alzheimer disease. Ann. Neurol. 79, 90–109.
Lai, A.Y., McLaurin, J., 2012. Clearance of amyloid-beta peptides by microglia and macrophages: the issue of what, when and where. Future Neurol. 7, 165–176.
Lebson, L., Nash, K., Kamath, S., Herber, D., Carty, N., Lee, D.C., Li, Q., Szekeres, K., Jinwal, U., Koren, J., Dickey, C.A., Gottschall, P.E., Morgan, D., Gordon, M.N., 2010. Trafficking CD11b-positive blood cells deliver therapeutic genes to the brain of amyloid-depositing transgenic mice. J. Neurosci Off. J. Soc. Neurosci. 30, 9651–9658.
Lund, S.A., Giachelli, C.M., Scatena, M., 2009. The role of osteopontin in inflammatory processes. J. Cell Commun. Signaling 3, 311–322.
Majumdar, A., Chung, H., Dolios, G., Wang, R., Asamoah, N., Lobel, P., Maxfield, F.R., 2008. Degradation of fibrillar forms of Alzheimer's amyloid beta-peptide by macrophages. Neurobiol. Aging 29, 707–715.
Malm, T., Magga, J., Koistinaho, J., 2012. Animal models of Alzheimer's Disease: utilization of transgenic Alzheimer's Disease models in studies of amyloid beta clearance. Curr. Transl. Geriatr. Exp. Gerontol. Rep. 1, 11–20.
Mawuenyega, K.G., Sigurdson, W., Ovod, V., Munsell, L., Kasten, T., Morris, J.C., Yarasheski, K.E., Bateman, R.J., 2010. Decreased clearance of CNS beta-amyloid in Alzheimer's disease. Science 330, 1774.
McWhorter, F.Y., Wang, T., Nguyen, P., Chung, T., Liu, W.F., 2013. Modulation of macrophage phenotype by cell shape. Proc. Natl. Acad. Sci. U.S.A. 110, 17253–17258.
Meller, R., Stevens, S.L., Minami, M., Cameron, J.A., King, S., Rosenzweig, H., Doyle, K., Lessov, N.S., Simon, R.P., Stenzel-Poore, M.P., 2005. Neuroprotection by osteopontin in stroke. J. Cereb. Blood Flow Metab. Off. J. Int. Soc. Cereb. Blood Flow Metab. 25, 217–225.
Patarca, R., Freeman, G.J., Singh, R.P., Wei, F.Y., Durfee, T., Blattner, F., Regnier, D.C., Kozak, C.A., Mock, B.A., Morse 3rd, H.C., et al., 1989. Structural and functional studies of the early T lymphocyte activation 1 (Eta-1) gene. Definition of a novel T cell-dependent response associated with genetic resistance to bacterial infection. J. Exp. Med. 170, 145–161.
Perrin, R.J., Fagan, A.M., Holtzman, D.M., 2009. Multimodal techniques for diagnosis and prognosis of Alzheimer's disease. Nature 461, 916–922.
Prokop, S., Miller, K.R., Drost, N., Handrick, S., Mathur, V., Luo, J., Wegner, A., Wyss-Coray, T., Heppner, F.L., 2015. Impact of peripheral myeloid cells on amyloid-beta pathology in Alzheimer's disease-like mice. J. Exp. Med. 212, 1811–1818.
Rittling, S.R., 2011. Osteopontin in macrophage function. Expert Rev. Mol. Med. 13, e15.
Rosa, P., Barr, F.A., Stinchcombe, J.C., Binacchi, C., Huttner, W.B., 1992. Brefeldin A inhibits the formation of constitutive secretory vesicles and immature secretory granules from the trans-Golgi network. Eur. J. Cell Biol. 59, 265–274.
Saido, T.C., 1998. Alzheimer's disease as proteolytic disorders: anabolism and catabolism of beta-amyloid. Neurobiol. Aging 19, S69–75.
Scatena, M., Liaw, L., Giachelli, C.M., 2007. Osteopontin: a multifunctional molecule regulating chronic inflammation and vascular disease. Arterioscler. Thromb. Vasc. Biol. 27, 2302–2309.
Schack, L., Stapulionis, R., Christensen, B., Kofod-Olsen, E., Skov Sorensen, U.B., Vorup-Jensen, T., Sorensen, E.S., Hollsberg, P., 2009. Osteopontin enhances phagocytosis through a novel osteopontin receptor, the alphaXbeta2 integrin. J. Immunol. (Baltimore, Md.: 1950) 182, 6943–6950.
Selkoe, D.J., 2001. Alzheimer's disease results from the cerebral accumulation and cytotoxicity of amyloid beta-protein. J. Alzheimers Dis. 3, 75–80.
Shankar, G.M., Li, S., Mehta, T.H., Garcia-Munoz, A., Shepardson, N.E., Smith, I., Brett, F.M., Farrell, M.A., Rowan, M.J., Lemere, C.A., Regan, C.M., Walsh, D.M., Sabatini, B.L., Selkoe, D.J., 2008. Amyloid-beta protein dimers isolated directly from Alzheimer's brains impair synaptic plasticity and memory. Nat. Med. 14, 837–842.
Shechter, R., London, A., Varol, C., Raposo, C., Cusimano, M., Yovel, G., Rolls, A., Mack, M., Pluchino, S., Martino, G., Jung, S., Schwartz, M., 2009. Infiltrating blood-derived macrophages are vital cells playing an anti-inflammatory role in recovery from spinal cord injury in mice. PLoS Med 6, e1000113.
Shin, Y.J., Kim, H.L., Choi, J.S., Choi, J.Y., Cha, J.H., Lee, M.Y., 2011. Osteopontin: correlation with phagocytosis by brain macrophages in a rat model of stroke. Glia 59, 413–423.
Simard, A.R., Soulet, D., Gowing, G., Julien, J.P., Rivest, S., 2006. Bone marrow-derived microglia play a critical role in restricting senile plaque formation in Alzheimer's disease. Neuron 49, 489–502.
Sun, Y., Yin, X.S., Guo, H., Han, R.K., He, R.D., Chi, L.J., 2013. Elevated osteopontin levels in mild cognitive impairment and Alzheimer's disease. Mediat. Inflamm. 2013, 615745.
Suzuki, H., Ayer, R., Sugawara, T., Chen, W., Sozen, T., Hasegawa, Y., Kanamaru, K., Zhang, J.H., 2010. Protective effects of recombinant osteopontin on early brain injury after subarachnoid hemorrhage in rats. Crit. Care Med. 38, 612–618.
Tambuyzer, B.R., Casteleyn, C., Vergauwen, H., Van Cruchten, S., Van Ginneken, C., 2012. Osteopontin alters the functional profile of porcine microglia in vitro. Cell Biol. Int. 36, 1233–1238.
Tan, T.K., Zheng, G., Hsu, T.T., Lee, S.R., Zhang, J., Zhao, Y., Tian, X., Wang, Y., Wang, Y. M., Cao, Q., Wang, Y., Lee, V.W., Wang, C., Zheng, D., Alexander, S.I., Thompson, E., Harris, D.C., 2013. Matrix metalloproteinase-9 of tubular and macrophage origin contributes to the pathogenesis of renal fibrosis via macrophage recruitment through osteopontin cleavage. Lab Invest. 93, 434–449.
Toyonaga, T., Nakase, H., Ueno, S., Matsuura, M., Yoshino, T., Honzawa, Y., Itou, A., Namba, K., Minami, N., Yamada, S., Koshikawa, Y., Uede, T., Chiba, T., Okazaki, K., 2015. Osteopontin deficiency accelerates spontaneous colitis in mice with disrupted gut microbiota and macrophage phagocytic activity. PloS One 10, e0135552.
van Velthoven, C.T., Heijnen, C.J., van Bel, F., Kavelaars, A., 2011. Osteopontin enhances endogenous repair after neonatal hypoxic-ischemic brain injury. Stroke 42, 2294–2301.
Varvel, N.H., Grathwohl, S.A., Degenhardt, K., Resch, C., Bosch, A., Jucker, M., Neher, J. J., 2015. Replacement of brain-resident myeloid cells does not alter cerebral amyloid-beta deposition in mouse models of Alzheimer's disease. J. Exp. Med. 212, 1803–1809.
Verhulst, A., Persy, V.P., Van Rompay, A.R., Verstrepen, W.A., Helbert, M.F., De Broe, M.E., 2002. Osteopontin synthesis and localization along the human nephron. J. Am. Soc. Nephrol. 13, 1210–1218.
Wung, J.K., Perry, G., Kowalski, A., Harris, P.L., Bishop, G.M., Trivedi, M.A., Johnson, S. C., Smith, M.A., Denhardt, D.T., Atwood, C.S., 2007. Increased expression of the remodeling- and tumorigenic-associated factor osteopontin in pyramidal neurons of the Alzheimer's disease brain. Curr. Alzheimer Res. 4, 67–72.
Wyss-Coray, T., 2006. Inflammation in Alzheimer disease: driving force, bystander or beneficial response? Nat. Med. 12, 1005–1015.
Wyss-Coray, T., Lin, C., Yan, F., Yu, G.Q., Rohde, M., McConlogue, L., Masliah, E., Mucke, L., 2001. TGF-beta1 promotes microglial amyloid-beta clearance and reduces plaque burden in transgenic mice. Nat. Med. 7, 612–618.
Yin, Z., Raj, D., Saiepour, N., Van Dam, D., Brouwer, N., Holtman, I.R., Eggen, B.J.L., Möller, T., Tamm, J.A., Abdourahman, A., Hol, E.M., Kamphuis, W., Bayer, T.A., De Deyn, P.P., Boddeke, E., 2017. Immune hyperreactivity of Aβ plaque-associated microglia in Alzheimer's disease. Neurobiol. Aging 55, 115–122.
Zuroff, L., Daley, D., Black, K.L., Koronyo-Hamaoui, M., 2017. Clearance of cerebral Abeta in Alzheimer's disease: reassessing the role of microglia and monocytes. Cell Mol. Life Sci. 74, 2167–2201.